PARYLENE-BASED WIRELESS INTRAOCULAR PRESSURE SENSOR FOR GLAUCOMA RESEARCH

By

Brian Crum

A THESIS

Submitted to
Michigan State University
in partial fulfillment of the requirements
for the degree of

Electrical Engineering – Master of Science

2013

ABSTRACT

PARYLENE-BASED WIRELESS INTRAOCULAR PRESSURE SENSOR FOR GLAUCOMA RESEARCH

By

Brian Crum

Direct, accurate, and continuous intraocular pressure (IOP) monitoring is necessary to better understand the relationship between elevated IOP and glaucoma, a degenerative eye disease. Currently, tonometry is used to measure IOP in research subjects. In this technique, the deflection of the cornea due to a known applied force is measured and IOP values are derived based on the invalid assumption that the corneas of all eyes are very similar. Tonometry is highly operator dependent, labor intensive and can be stressful to research animals, particularly if a study calls for several daily measurements. This thesis describes the development of a wireless, implantable pressure sensor that can overcome these drawbacks of traditional IOP monitoring. Design, fabrication and characterization of the Parylene-based sensor are presented with the aim of enabling 1-2 year studies on the relationship between IOP and glaucoma. The sensor is comprised of an integrated planar MEMS coil and a capacitive pressure sensing element. Parylene-C was chosen as the packaging and structural material due to its flexibility and performance as a moisture and dielectric barrier. Sensors were evaluated for sensitivity and telemetry distance in an environment approximating the anterior chamber of the eye. Experimental results demonstrate wireless pressure sensing capability with 1 mmHg resolution over the range of 0-100 mmHg in isotonic saline at a telemetry distance of 20 mm.

Copyright by BRIAN CRUM 2013

TABLE OF CONTENTS

LIST OF TABLES	vi
LIST OF FIGURES	vii
CHAPTER 1: INTRODUCTION	1
CHAPTER 2: BACKGROUND	6
2.1 Glaucoma	7
2.2 Tonometry	9
2.2.1 Indentation Tonometry	10
2.2.2 Applanation Tonometry	11
2.2.3 Rebound Tonometry	13
2.2.4 Dynamic Contour Tonometry	14
2.3 Continuous IOP Sensing in Lab Animals	
2.4 Implantable IOP Sensors State of the Art	18
2.5 Summary	23
CHAPTER 3: DESIGN AND SIMULATION	
3.1 Sensor Design	
3.1.1 Capacitive Sensing	
3.1.2 Inductive Coupling	
3.1.3 Resistance, Quality Factor and Coupling Efficiency	
3.1.4 Parasitic Effects	
3.2 RLC Resonance	38
3.3 Impedance Phase Dip Technique	
3.4 Conclusion	42
CHAPTER 4: VERSION I SENSOR	43
4.1 Design Goals	
4.2 Design and Fabrication	
4.3 Testing Procedures and Results	
4.4 Remaining Challenges	
4.4.1 Biocompatible Materials and Interface Sealing	
4.4.2 Flexibility	
4.4.3 Performance	
4.5 Conclusion	
CHAPTER 5: VERSION II SENSOR	
5.1 Version I Sensor Challenges and Solutions	
5.1.1 Sealing of the Fold-and-Bond Interface	
5.1.2 Flexibility	56

5.1.3 Biocompatibility	57
5.1.4 Overall Sensor Performance	
5.2 Sensor Design	58
5.2.1 Sensor Properties	
5.3 Testing Setup and Results	
5.4 Summary of Results and Conclusion	
CHAPTER 6: CONCLUSION AND OUTLOOK	67
6.1 Readout Unit	67
6.2 Remaining Challenges	69
6.3 Potential for Human Implantation	
APPENDICES	72
Appendix A	
Appendix B	76
BIBLIOGRAPHY	79

LIST OF TABLES

Table 2-1. A summary of recently developed implantable intraocular pressure sensors		
Table 3- 1. Effect of dielectric medium on sensor response	. 38	
Table 4- 1. Design specifications for the version I sensor	. 44	
Table 4- 2. Theoretical and Measured Version 1 Sensor Characteristics	. 47	
Table 4- 3. Summary of results for version I sensor testing	. 50	
Table 5- 1. Theoretical sensor characteristics	. 61	
Table 5- 2. Summary of results	. 66	

LIST OF FIGURES

Figure 1- 1. Concept diagram for a wireless IOP sensor. A) readout unit. B) reader coil. C) sensor implanted in the anterior chamber of the eye. D) the eye. For interpretation of the references to color in this and all other figures, the reader is referred to the electronic version of this thesis.	
Figure 2- 1. a) Peripheral retinal ganglion cells and their location in the eye. b) The effect of peripheral retinal ganglion cell loss on the visual field.	6
Figure 2- 2. Normal aqueous humor production and drainage. Adapted from [8]	8
Figure 2- 3. Schiotz tonometer. From [12]	10
Figure 2- 4. Goldman tonometry in use, and the fluorescent rings visible through the biomicroscope. From [19]	.12
Figure 2- 5. Rebound tonometer in use. From [27]	14
Figure 2- 6. The PASCAL tonometer in use. From [29]	15
Figure 2- 7. The Bourdon tube demonstrates the underlying concept of the sensor described in [47]. From [48]	
Figure 2- 8. The Wireless Intraocular Transducer and wireless readout unit (WIT). From [7]	23
Figure 3- 1. MEMS capacitive pressure sensing element	28
Figure 3- 2. Effective dielectric constant for multiple dielectric layers	29
Figure 3- 3. Single-turn inductor	32
Figure 3- 4. Equivalent circuit for overall sensor capacitance	34
Figure 3- 5. Cross-Section of a two-turn coil used for COMSOL simulation	36
Figure 3- 6. Coil parasitic capacitance versus depth of dielectric medium	37
Figure 3- 7. Equivalent circuit for the sensor	39
Figure 3- 8. Inductive coupling between reader and sensor coils for phase dip telemetry	40
Figure 3- 9. PSPICE simulation illustrates the importance of weak inductive coupling	41
Figure 4- 1 Fabricated Sensor (a) before and (b) after bonding	46

Figure 4- 2. Water testing setup for version I sensor	48
Figure 4- 3. Results of water pressure testing	49
Figure 4- 4. Pressure sensor frequency response to different media	50
Figure 4- 5. Flexibility of the version I sensor	52
Figure 5- 1. Patterned photoresist	56
Figure 5- 2. Melting photoresist interface	56
Figure 5- 3. Parylene coating	56
Figure 5- 4. Resistance to creasing when folded in toward Parylene support structure	56
Figure 5- 5. Sensor dimensions.	59
Figure 5- 6. COMSOL simulation of inductor magnetic field	61
Figure 5- 7. Deflection of the capacitive sensing membranes due to an applied pressure	62
Figure 5- 8. Simulated capacitance versus pressure	63
Figure 5- 9. Simulated chamber deflection versus pressure	63
Figure 5- 10. Experimental setup for testing in (a) air and (b) water. (c) Reader coil and test chamber	64
Figure 5- 11. Frequencies at which phase dip minimum occurs as seen in figure 5-11. Data for pressures from 0 and 100 mmHg above atmospheric pressure in air (left) and water (right)	
Figure 5- 12. Measured impedance phase curves in air (left) and liquid (right) media	65
Figure B- 1. Patterned AZ4620 photoresist	76
Figure B- 2. Fold-and-bond technique	77
Figure B- 3 Device after elimination of photoresist interface by melting	77

CHAPTER 1: INTRODUCTION

Glaucoma is a degenerative eye disease usually associated with elevated intraocular pressure (IOP) that causes progressive vision loss. It afflicts 60 million people worldwide and has caused severe visual impairment or blindness in 9 million [1]. The pathophysiology of glaucoma is extremely complex and current methods to diagnose and treat it are not always effective. Many drugs and surgeries have been developed to lower average IOP to ease the symptoms of glaucoma but recent research suggests that controlling the range of IOP fluctuations might be of greater therapeutic benefit [2]. A normal diurnal IOP cycle can range from 12-21 mmHg. In glaucomatous eyes, fluctuations can be much greater and, as has recently been demonstrated in primary open-angle glaucoma (POAG) patients, peaks can occur at night while a patient is sleeping [3]. Currently available indirect sensors such as the Sensimed Triggerfish®, which is built into a contact lens, are capable of 24-hour IOP monitoring and treatments are already being tailored to treat peak IOP values when they occur and to limit IOP fluctuation. These approaches to glaucoma treatment are very new and still based on an incomplete understanding of the disease process. Research is needed to understand the diurnal IOP cycles now being observed in glaucoma patients. New studies must be designed wherein continuous, accurate IOP monitoring of laboratory animals will be of vital importance. The large variety of glaucoma types and pathogeneses suggest a great number of studies must be conducted to provide a complete picture of the disease. Expensive, complex, inaccurate or labor intensive IOP monitoring systems will not allow this research to progress at a pace befitting the severity of the problem. The goal of this research is to develop a wireless, implantable, biocompatible

pressure sensor capable of in vivo IOP measurement. In addition, our goal is that the sensor will be practical for 1-2 year large-scale glaucoma studies involving research animals.

Key factors that were considered in the design of this device are size, cost and complexity of fabrication, sensitivity, implantation difficulty, biocompatibility, and ease of telemetry. Long-term stability was also a major consideration. To begin, it was determined that a readout system should be able to function at a distance of two centimeters or more from the sensor. This is a typical glasses-to-pupil distance in humans and would enable continuous IOP monitoring with a reader unit incorporated in specially designed goggles to be worn by research animals. It was determined that this goal could be met by absolute passive sensors or by active or RFID based sensors.

Passive sensors became the focus of this work for a few reasons. Cost and fabrication complexity can be far lower in a passive device. Passive devices can be constructed entirely from biocompatible materials; a packaging failure in such a device does not have the potential to harm a research subject. Passive devices are simpler in principle and can be made very rugged and flexible. Active or RFID devices require at least portions of the implant to be rigid and often fragile. Materials used in these devices generally have poor chemical resistance. Another key concern is ease of implantation. Surgical procedures to implant a sensor should be minimally invasive and easy to perform. Large-scale studies require the surgery to be performed several times, so lengthy and difficult procedures would require a great deal of time and expense to prepare subjects. Invasive surgical procedures are also possible sources of error in a study.

Glaucoma is a common complication in both humans and animals after invasive eye surgeries [4-5]. It may be difficult to study the pathogeneses of glaucoma in research animals if, through

surgical implantation of an intraocular pressure sensor, glaucoma of various and unknown severity was actually caused in the research subject.

Energy efficiency is an additional benefit to selecting a passive device, in which the sensors consume no energy, and wireless inductive powering allows for very low coupling efficiency and limited transmission distance. For active devices in which the sensors themselves consume energy, battery replacements require invasive surgeries causing potential harm to subjects or patients and introducing potential sources of error into studies.

Two very important factors to minimize and control surgical risk are the sensor placement upon implantation and the incision size. Small incisions are possible with very small rigid devices or large, flexible devices. All devices must be secured in place upon implantation. Larger, flexible intraocular implants that are placed in the anterior chamber can be angle-supported. That is, the outer edges of the device can safely press against the interface of the iris and the cornea. They can be implanted using well-established surgical procedures currently in use for flexible phakic intraocular lenses [6] or simply by folding and inserting the sensor with forceps just as the Wireless Intraocular Transducer (Implandata Opthalmic Products GmbH) is implanted [7]. Smaller devices however must be anchored or sutured in place. This can complicate the implantation procedure and create difficulties if the sensor must later be removed. If the sensor break free after implantation it can cause damage as it moves through the eye.

A concept diagram for the inductively coupled wireless intraocular pressure sensor is shown below in Figure 1-1. The portable unit with attached reader coil is held roughly two centimeters from the sensor implanted in the eye. A variable oscillator energizes the reader coil which couples inductively with the sensor. The sensor consists of a capacitive pressure sensing chamber and planar inductor, forming an LC circuit with a resonant frequency that depends on

the pressure exerted on the capacitive sensing chamber. The resonant frequency of the sensor is determined using the impedance phase dip technique.

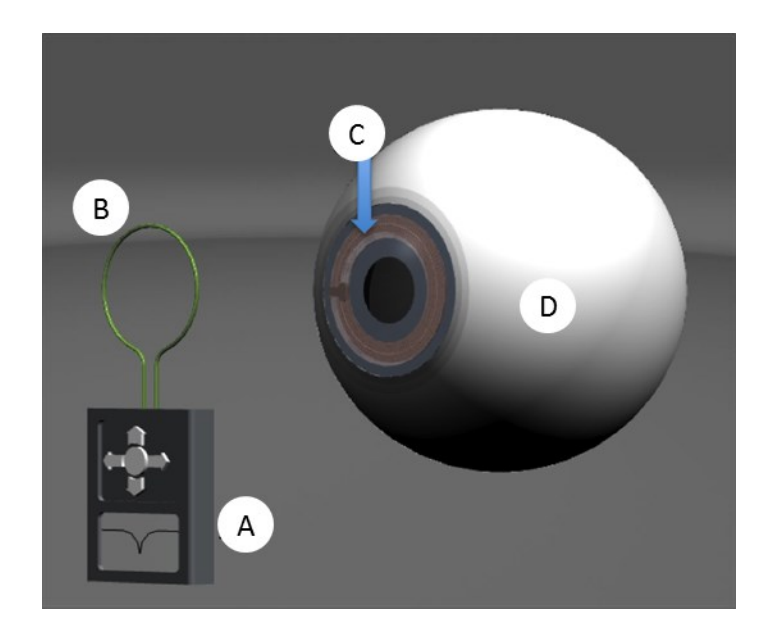


Figure 1-1. Concept diagram for a wireless IOP sensor. A) readout unit. B) reader coil. C) sensor implanted in the anterior chamber of the eye. D) the eye. For interpretation of the references to color in this and all other figures, the reader is referred to the electronic version of this thesis.

The impedance phase dip technique was chosen as the telemetry method for this inductively coupled passive sensor. In this technique, the impedance phase of a reader coil held coaxial to the sensor is read over a frequency range of interest. If inductive coupling between the reader coil and sensor is weak, a dip occurs in the measured impedance phase at approximately the resonant frequency of the sensor. While this technique does not measure the true resonant frequency of the sensor, its accuracy increases as inductive coupling efficiency decreases. This means that the reader coil can and should be held at the maximum distance from the sensor possible while still able to detect a phase dip.

This thesis is structured as follows: Chapter 2 will begin with a review of glaucoma, its relationship to IOP and the history of IOP measurement. Current direct pressure sensing schemes will be discussed including state-of-the-art wireless pressure sensing. The benefits and drawbacks of each IOP measurement method will be outlined with an emphasis on their usefulness to glaucoma research. In Chapter 3, the concepts used to design and characterize the wireless IOP sensors presented in this thesis will be discussed. Chapter 4 will focus on the first iteration of the pressure sensor. Its performance, benefits and flaws will be discussed in detail. Chapter 5 covers the current version of the sensor, with an emphasis on overcoming the challenges from the previous version. Simulation results will be presented here and will be compared to measured data. Chapter 6 is the conclusion and future outlook. A brief conclusion reviews the achievements of this work and the challenges that remain. The outlook section discusses the work necessary to develop a fully functional IOP sensing platform based on the types of sensors discussed in Chapters 4 and 5. Also discussed are different directions this work could take in the future and which of these are likely to be most impactful on the broader goal of understanding and developing treatments for glaucoma.

CHAPTER 2: BACKGROUND

Glaucoma is a group of devastating degenerative eye diseases with complex and multi-factorial pathogeneses that are not fully understood. Glaucoma causes a loss of function in the optic nerve that can be slowed or halted by decreasing the pressure within the eye. In glaucoma there is a consistent and well-defined relationship between elevated intraocular pressure (IOP) and progression of the disease. The disease affects retinal ganglion cells (Figure 2-1a), which are the last link in the visual pathway of the retina. The axons of these cells bundle together at the back of the eye to form the optic nerve. Retinal ganglion cells are very sensitive to prolonged elevation and fluctuation of IOP. Ganglion cell death in a glaucomatous eye first occurs at the periphery of the retina, causing a narrowing of the visual field (Figure 2-1b). As the disease progresses the visual field narrows further, eventually causing total blindness.

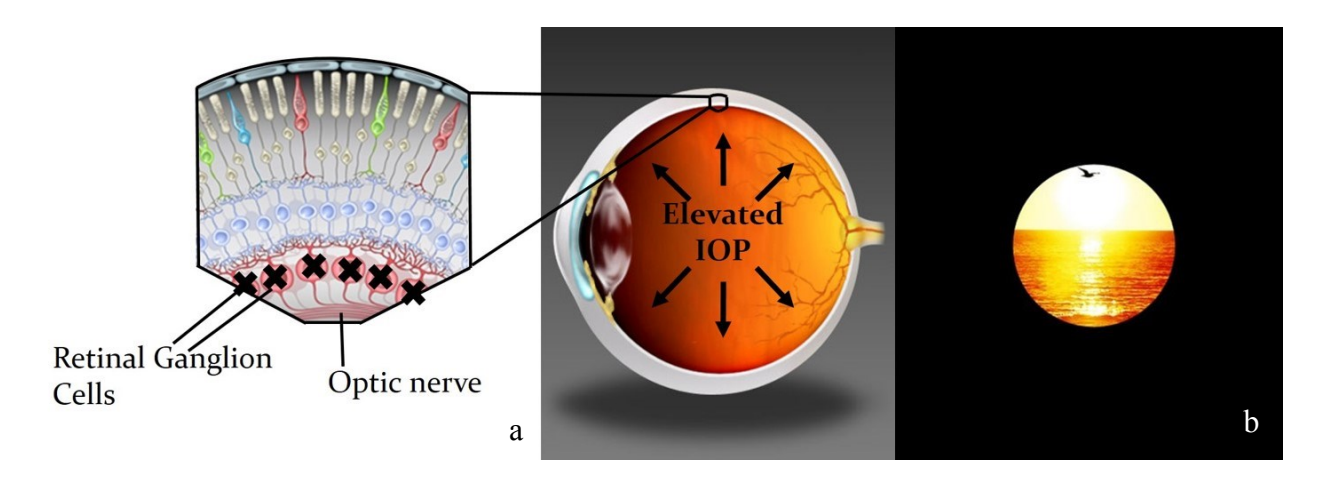


Figure 2-1. a) Peripheral retinal ganglion cells and their location in the eye. b) The effect of peripheral retinal ganglion cell loss on the visual field.

Established treatment protocols for glaucoma show that decreasing IOP impedes or arrests progression of the disease, and accurate timely IOP measurements provide invaluable prognostic information for vision and comfort. This makes IOP the main target for glaucoma therapy today.

Because IOP is the main target for glaucoma therapy, it is of great interest for further research. Abnormally high levels of aqueous humor, the liquid medium that fills the anterior chamber of the eye and supports the curvature of the cornea, is the cause of elevated IOP in glaucomatous eyes. In a normal eye, the production of aqueous humor is nearly equivalent to its outflow, maintaining IOP in the range of 10-21 mmHg. In human patients with glaucoma, the intraocular pressure at the time of diagnosis can range from pressures within the reference interval of 10-21 mmHg to over 50mmHg. Elevations in IOP occur when there is an increased production of aqueous humor, a decreased outflow, or both.

2.1 Glaucoma

Figure. 2-2 shows the normal production and flow of aqueous humor in a healthy eye. Aqueous humor is produced by the ciliary body in the posterior chamber of the eye. It circulates through the posterior and anterior chambers, and then exits by one of two pathways. The first is through the trabecular meshwork that lines the anterior chamber angle. From the trabecular meshwork, aqueous humor exits the eye through Schlemm's canal and is absorbed into the bloodstream in the episcleral veins. The second route is known as the unconventional pathway, where aqueous humor exits the eye through the uveoscleral tract. While only a small percentage of aqueous humor outflow uses this route, recent research suggests it is very important to

maintaining healthy IOP. A recent study found that uveoscleral outflow stops entirely during sleep in 70% of primary open angle glaucoma (POAG) patients, causing a diurnal maximum in IOP. This discovery has been useful to ophthalmologists in directing the use of medication for POAG patients [7].

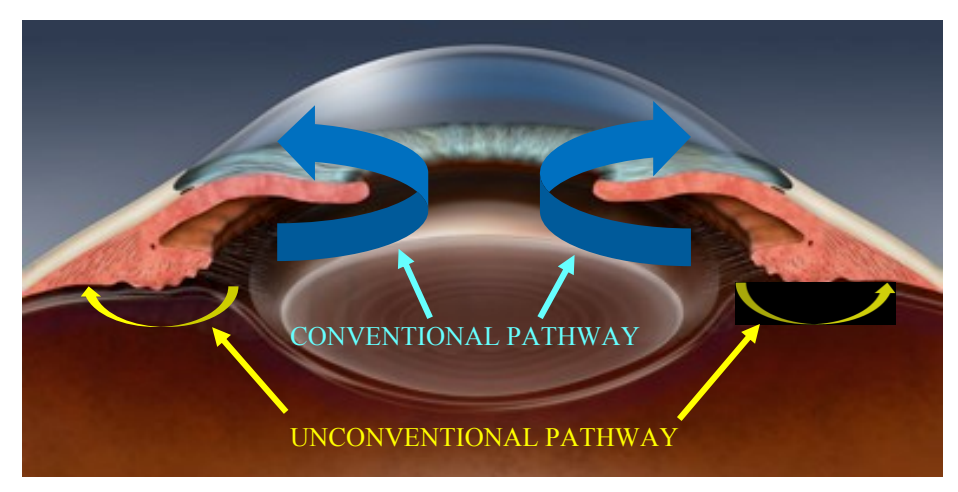


Figure 2- 2. Normal aqueous humor production and drainage. Adapted from [8]

Modern glaucoma diagnosis, monitoring, and treatments are almost entirely focused on maintaining IOP in the range that slows or stops progression on the disease. For the majority of patients, this means keeping IOP within the range of 10-21 mmHg [9]. Maintaining a healthy IOP in a glaucomatous eye is very challenging. There are no natural mechanisms to inhibit the production of aqueous humor when IOP deviates above healthy levels.

Without a natural control mechanism, ophthalmologists must try to control IOP with pharmaceutical and surgical interventions. Currently, the vast majority of available medical treatments either reduces aqueous humor production or increases the rate of aqueous humor outflow [9]. Choosing which treatments are appropriate is a very challenging proposition. One-third of all glaucoma patients (two-thirds in Japan) have IOP measurements consistently below 21 mmHg [10]. This condition is called normal tension glaucoma (NTG). The treatment for

NTG, like all forms of glaucoma, is to limit the progression of the disease by decreasing IOP. Generally an ophthalmologist will begin lowering IOP with the least invasive pharmaceutical treatments. If the disease continues to progress, surgical options are used. The IOP at which no further structural or functional disease progression is noted is the correct IOP for that patient. Determining the correct IOP in this way can be very costly. The expense, pain and vision loss incurred while the disease is actively progressing are irreversible and can be devastating to patients. To mitigate suffering caused by glaucoma, research is needed to better understand how glaucoma develops, progresses, and responds to various treatments.

2.2 Tonometry

It is well known that modern IOP measurements are not accurate. Several studies have concluded that tonometry IOP measurements differ greatly among patients due to their different corneal properties [11]. Equipment to measure corneal thickness can provide correction factors for better accuracy. Still, other properties that are more difficult to measure such as corneal elasticity and tear film characteristics ensure tonometry will remain an imprecise science. However, comparing tonometry reading of a single patient over time can be very useful. Although corneal properties change with age, on a sufficiently short time-scale it can be assumed that no corneal change has occurred, and changes to tonometry readings strongly indicate fluctuations in IOP.

Methods of clinical tonometry developed over the past century have relied upon measurements of the corneal surface to extrapolate the IOP. These methods can be categorized

broadly as indentation tonometry, applanation tonometry, rebound tonometry, and dynamic contour tonometry.

2.2.1 Indentation Tonometry

Von Graefe first formally described indentation tonometry in 1862. The underlying principle applies a known weight to the corneal surface and measures the deformation, which will be lessened by elevated IOP. Indentation tonometry continued to develop through the late 19th century, and Schiotz developed a refined mechanical indentation tonometer in 1905. The Schiotz tonometer is the only indentation device still in widespread use today. It consists of a curved footplate and weighted plunger attached to a lever and scale, as shown in Figure 2-3. The eye undergoing measurement must be horizontal, as the tonometer relies upon gravity to apply a known force to the weighted plunger when the footplate is rested on the surface of the cornea. Each 50 µm that the plunger sinks below the footplate translates into one scale unit on the tonometer.



Figure 2- 3. Schiotz tonometer. From [12]

The Schiotz tonometer was originally calibrated using manometry studies in human cadaver and artificial eyes [13-15]. The calibration of the Schiotz scale and translation to intraocular pressures does not account for differences in scleral rigidity. In myopic subjects the intraocular pressure will be underestimated, while in subjects with hyperopia or corneal scarring the intraocular pressure will be overestimated [16]. The Schiotz tonometer also requires either complete subject cooperation or restraint along with the application of a topical anesthetic. It is user-dependent and more subject to external sources of error than other methods of indirect tonometry. External sources of error during tonometry include eye movements, increased venous pressure due to pressure on the neck and pressure on the eyelids [17-18].

2.2.2 Applanation Tonometry

Applanation tonometry was proposed by Weber in 1867, then further studied and developed by Imbert and Fick. Applanation tonometry is based upon the relationship now known as the Imbert-Fick Law, which states that the pressure within a perfect sphere is approximately equal to the external force required to flatten the sphere divided by the area flattened. Malakoff developed a fixed force tonometer based on this principle, which relied on dyes to mark the area of the cornea applanated to calculate the intraocular pressure. This method was extremely vulnerable to error from even slight eye movements or variability in tear film.

In 1955, Goldman developed a fixed area variable force tonometer, which became the gold standard for tonometry and remains so today. Goldman determined that at an applanated circular area of diameter 3.06 mm, the force of corneal rigidity which causes an overestimation of intraocular pressure, and the force of the tear film, which causes an underestimation of

intraocular pressure, are equal and opposite. Goldman's tonometer consists of a circular applanating surface of 3.06 mm in diameter attached to an arm controlled by a spring-loaded knob for applying a known force. As shown in Figure 2-4, this setup is mounted to a slit-lamp biomicroscope and requires the use of a topical anesthetic and fluorescein stain. The applanating surface contacts the cornea, creating a ring of fluorescence visible through the biomicroscope. The force can then be adjusted until the applanating surface is in complete contact with the cornea. The mass in grams used to create the applanating force multiplied by 10 is the intraocular pressure in mmHg. For example, 1.4 g of mass corresponds to an IOP of 14 mmHg.



Figure 2- 4. Goldman tonometry in use, and the fluorescent rings visible through the biomicroscope. From [19]

When calibrating his tonometer, Goldman used an average central corneal thickness of 500 µm, and his method does not allow for variations in corneal thickness. Recent studies have shown that intraocular pressure readings obtained by Goldman Applanation Tonometry differ from readings collected by manometry by 0.25 mmHg for every 10 µm change in central corneal thickness [20-21]. Goldman applanation tonometry is also affected by astigmatism, corneas which have undergone refractive surgical procedures, corneal scarring or edema, irregular

corneal surfaces, variable volumes or concentrations of fluorescein stain, and variable scleral rigidity, all of which can introduce significant error to this method of measurement.

Several devices are in widespread use clinically today as screening tools to approximate intraocular pressure. These are combination indentation and applanation devices, and include the portable TonoPen XL® and pneumotonometers, which use a puff of air to deform the eye. Both devices correlate well with the Goldman tonometer within mid-range values for intraocular pressure, but begin to have more variability at very low or very high pressures. In addition, both devices are affected by corneal shape and refractive surgical procedures, which continue to provide significant sources of error [21].

2.2.3 Rebound Tonometry

In rebound tonometry, the motion of a probe bounced off the surface of the cornea is analyzed and correlated intraocular pressure. Obbink first proposed the concept of rebound tonometry in 1937, and Obbink et al. were the first to put the concept into practice for research purposes in 1967. Rebound tonometry has reached widespread clinical use via the iCARE tonometer developed jointly at the University of Helsinki in Finland and Mount Sinai Medical School in the United States in 1997. The tonometer consists of a stainless steel projectile probe with disposable plastic caps for individual use, an extension spring, and a microprocessor. The probe bounces off the corneal surface, and the microprocessor analyzes the deceleration of the probe. A higher rate of deceleration indicates higher intraocular pressure. The size of the iCARE probe and the force involved are small enough that it can be used without topical anesthesia. The instrument (Figure 2-5) is an easy to use handheld portable device. In one study, when used to

measure IOP in healthy eyes, the iCARE tonometer overestimated the values by an average of 1.34 mmHg compared to Goldman Applanation Tonometry [22]. Several studies have reported that the iCARE system is inaccurate with differing central cornea thickness values as compared to Goldman Applanation Tonometry, and had worse repeatability [23-26].



Figure 2- 5. Rebound tonometer in use. From [27]

2.2.4 Dynamic Contour Tonometry

Dynamic Contour Tonometry is the first indirect method of IOP measurement that is theoretically not affected by structural differences in the sclera and cornea. Kanngeiser et al. developed this method for research purposes and published their findings in 2005 [28]. Their work paved the way for the development of the PASCAL tonometer now available for clinical use, as shown in Figure 2-6.

Dynamic contour tonometry uses a specialized probe designed to match the contour of the typical human cornea, and contains a piezoelectric pressure sensor in the center of the probe.

The PASCAL tonometer is mounted to a slit lamp biomicroscope for verification of the interface between the cornea surface and the tonometer probe. The theory of its operation is based on perfect contour matching between the probe and the surface of the cornea. Under this condition, the equation: $F_{iop} + F_c + F_r + F_{ap} = 0$ is valid. Where F_{iop} is the intraocular pressure, F_{ap} is a constant appositional force that maintains the probe in contact with the cornea, and $F_c + F_r$ are opposing forces dues to adhesion and corneal rigidity respectively.



Figure 2- 6. The PASCAL tonometer in use. From [29]

IOP measurements obtained in the research setting by Kanngeiser et al. corresponded with reference values obtained from human cadaver eyes [28]. The PASCAL tonometer obtains values that correspond well with Goldman Applanation Tonometry values [30]. Several studies show that the accuracy and precision of the PASCAL tonometer are less dependent upon corneal thickness, age of the subject, and refractive surgical procedures than Goldman Applanation

tonometry [31-34]. Further investigation is needed to determine the effects of corneal hydration and corneal surface irregularities on dynamic contour measurements. Additional downfalls to the PASCAL tonometer include the need for a biomicroscope and the need for the subject to remain motionless with a steady eye and head position for five full seconds in order to obtain a suitable reading.

2.3 Continuous IOP Sensing in Laboratory Animals

All of the discussed tonometry methods have benefits and drawbacks, and none is ideal. To the author's best knowledge and although there are several promising candidates, there is not yet a commercially available IOP measurement platform for the practical continuous measurement of IOP in a large-scale animal study.

One critical shortcoming of tonometry in ocular hypertension and glaucoma research is that it is impractical to measure IOP changes within a day. It is well known that IOP fluctuates greatly throughout the day in a normal eye; a normal diurnal cycle can range from 10 mmHg to 21 mmHg. Manometric studies have established a normal diurnal cycle in over 30 genetic strains of mice to be between 20-30 mmHg [35]. In a study of DBA/2J mice, a strain of mice predisposed to angle closure glaucoma, IOP measurements in subjects with glaucomatous lesions ranged between 8 and 36mmHg when measured directly via microneedle cannulation [36]. In a study of 500 dogs including 30 breed variations, the mean IOP in healthy eyes was 19 mmHg with a range of 11-29 mmHg, and the IOP range in a colony of beagles with glaucoma ranged between 30 and 35 mmHg [37]. This cycle varies among different eyes and its relationship to different types of glaucoma is not fully understood. Aware that these daily fluctuations exist, an

ophthalmologist may diagnose ocular hypertension in a patient with an IOP reading below 21 mmHg depending on the time of day and their predictions about that patient's diurnal cycle.

Recently, a device built into a contact lens capable of recording a patient's diurnal cycle has been developed [38]. As this sensor comes into widespread use, new data will be available to ophthalmologists to help tailor treatment plans to patients' needs. New studies suggest that diurnal fluctuations in IOP may be more important to the progression of the disease than abnormally elevated IOP [39]. Research is needed to understand the diurnal IOP cycle and the relationship it may have to the onset and progression of glaucoma.

Another promising development in the treatment of glaucoma is the development of neuroprotective drugs. This area of research has identified several endogenous factors released in the visual pathway after an injury to promote healing, and has used these same compounds in an attempt to increase healing in eyes affected by elevated intraocular pressures. There has been evidence of accelerated healing and improved long-term function of visual pathway neurons with injections of such compounds, and even better healing with the use of long-term slow release delivery systems such as stem cells or viral vectors [40]. Accurate, continuous IOP monitoring would be extremely useful to evaluate the effectiveness of these therapies in eyes under known pressure conditions.

Research previously conducted on laboratory animals has often been hampered by the difficulty of obtaining accurate continuous IOP measurements. In a study conducted by Makoto et al. laboratory mice had their direct IOP read continuously from manometers connected to their eyes via cannulation [41]. This requires complete immobility of the research subject while measurements are recorded, and thus the mice were anesthetized during this process. The stress,

restraint, and anesthesia involved with this process introduce potential sources of error into the study.

A logical approach to overcoming these difficulties in future glaucoma research is the use of a wireless, implantable pressure sensor. Several such devices have been proposed but, to the best of the author's knowledge, have not yet been implemented in large-scale animal studies of glaucoma and ocular hypertension. An implantable sensor can provide direct pressure measurements for much improved accuracy. A well-designed experimental setup would eliminate the need to handle research animals in order to take IOP measurements. This could decrease labor-hours necessary to complete a study, reduce stress in research subjects as a source of experimental error and improve research animal welfare. Wireless measurements can be made continuously over the course of a study with information transmitted to a central computer for real-time analysis. The motivation for this thesis is to develop such a sensor at a cost that would not be prohibitive for most research budgets.

2.4 Implantable IOP Sensors State of the Art

There have been several attempts to construct an implantable intraocular pressure sensor.

These are summarized below in Table 1. All implantable pressure sensors are capable of direct measurement. Most implantable IOP sensors measure capacitance changes caused by pressure acting on a capacitive sensing chamber but some novel techniques have also been developed.

Wireless IOP sensors can be classified into two broad categories: active and passive.

Passive sensors include RFID devices that share some of the features and disadvantages of active devices. A further distinction is then needed for absolute passive sensors. These sensors are

generally simpler and cheaper than active and RFID devices. The aim of absolute passive IOP sensors, like the one presented in this thesis, is to transfer as much of the complexity associated with IOP measurement and recording outside of the eye. Thinking about wireless IOP sensors in this way can enable the development of low-cost sensing platforms where one very sophisticated readout unit could interface with several cheap, passive sensors. Without the need for integrated circuits or embedded power sources, these devices can be made entirely from biocompatible materials.

Active sensors allow the best sensitivity and telemetry distance at a much smaller size than passive devices. Integrated circuits are incorporated into these sensors to better detect subtle capacitance or resistance fluctuations, convert readings to digital values and transmit the acquired data to external readers. A main drawback of these sensors is their packaging requirements. Many elements of integrated circuits are not biocompatible and they must be hermetically packaged to prevent damage to the eye. The ocular environment is very harsh on electronics as well. Without hermetic packaging, active IOP sensors would become damaged with minimal exposure to the environment of the eye. Active sensors also need some type of energy source to function, which adds further sources of error to an already complex system.

Table 2-1. A summary of recently developed implantable intraocular pressure sensors

	Size	Active/	Sensing	Telemetry	Responsivity	Frequency at	D:-:4
	(mm^3)	Passive	Method	Distance	kHz/mmHg	$\Delta P=0 \text{ (MHz)}$	Rigid
[42]	N/A	passive	capacitive	2.5 cm	205	379	Partial
[43]	1.5	active	capacitive	50 cm	N/A	N/A	Yes
[44]	8.2	passive	capacitive	N/A	15	63	Yes
[45]	4.9	passive	capacitive	6 mm	1083	250	Somewhat
[46]	20.3	passive	capacitive	3 mm	160	481	Yes

Among the passive sensors in this table, the work in [45] stands out for excellent pressure sensitivity at a low frequency. SU-8 was chosen as the structural and packaging material. These layers of SU-8 are very flexible, making it a good choice for the structural material of a capacitive diaphragm. A possible difficulty with this design is the fragility of very thin SU-8 layers. The sensing distance achieved in this work is fairly low but could be improved with a larger coil.

A few wireless pressure sensors have been developed that do not sense capacitance change. In [47], an entirely unpowered, optically read pressure sensor was developed. The sensor functions like a Bourdon tube pressure gauge shown in Figure 2-7.

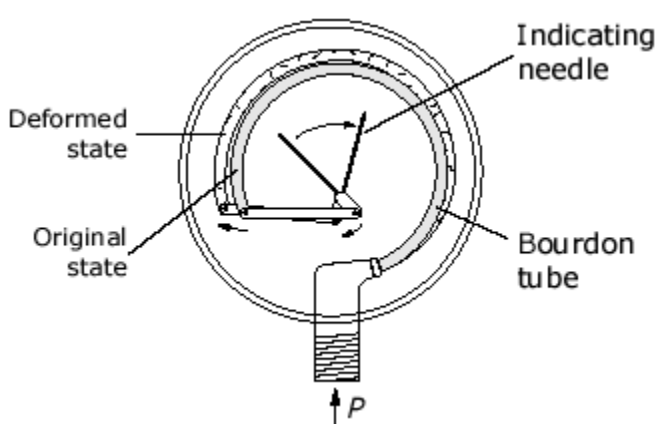


Figure 2- 7. The Bourdon tube demonstrates the underlying concept of the sensor described in [47]. From [48]

A Bourdon tube flattens slightly when the pressure inside the tube exceeds pressure outside. The greatest deflection occurs at the tip of the Bourdon tube, which is connected to an indicating needle. The research in [47] applies the same principle to a long spiral of Parylene tubing. The tubing is sealed on both ends and is anchored in the center of the spiral. The outer

end of the spiral is connected to an indicating needle that moves with changes in pressure. When implanted in an eye, the IOP can be read by comparing the tip of the indicating needle to marks on a nearby scale.

An interesting innovation in absolute passive capacitive sensors is presented in [42]. The sensor consists of a MEMS planar coil surrounding a circular capacitive sensing chamber. A capillary tube is fixed to one side of the device with access to the sensing chamber. The device is implanted outside the eye with only the capillary tube penetrating into the vitreous body. The vitreous body makes up the majority of the volume of the eye. It is filled with a thick, optically clear gel-like substance called vitreous humor. Pressure from the vitreous acts on the capillary tube causing movement is the flexible diaphragm outside the eye. Since the diaphragm is exposed to atmospheric pressure, its deflection depends on the difference between IOP and atmospheric pressure. Furthermore, implantation here allows an excellent sensing distance and a smaller coil size because the inductive coupling on which telemetry for this device depends, is not as hampered by the lossy material of the eye. Further study is needed to determine the validity of this approach. Because it rests on the surface of the eye, force from the tear film and eyelid acting directly on the device must be evaluated. While this sensor provides excellent sensitivity and telemetry distance, these forces may affect readings in practical applications. Also of concern is the comfort level associated with this device. If research animals find it irritating, they may try to remove it. This could require additional restraint, minimizing some of its advantages of this sensor over traditional manometry studies.

Inductive sensing elements have also been explored [49-50]. In [49], the distance of a ferrite material to a planar inductor varies with pressure. As the ferrite material moves closer to the inductor, the effective inductance of the system increases. The variable inductor is connected

with capacitors to form a resonator. An increase of inductance causes a decrease in the total system resonant frequency. The device presented in [50] uses the principal of mutual inductance between two coils placed coaxially. The mutual inductance of the system varies with coupling efficiency between the coils, which increases when the space between coils decreases due to pressure.

One RFID device in late stage of development shows promising results for human implantation [7]. This device (pictured below) uses sophisticated RFID technology to provide telemetry at distances up to 5 cm. Application specific integrated circuit developed for this device enables the detection of very small capacitance changes of the integrated capacitive sensor. The system uses a hand-held reader coil (Figure 2-8) where IOP can be read with 0.1 mmHg resolution.

The device is intended for human implantation during cataract surgery. It is implanted in the posterior chamber of the eye and is not intended to be implanted without removal of the natural lens. The sensor is 900 μ m thick and is 11.3 mm in diameter and is encapsulated in biocompatible silicone. Studies in animal and human subjects show the device is tolerated very well.



Figure 2- 8. The Wireless Intraocular Transducer and wireless readout unit (WIT). From [7]

2.5 Summary

There are many approaches to solving the problem of continuous IOP monitoring. Water column manometers are the most accurate of these approaches and are very useful as a calibration standard for new sensors. While several laboratory studies throughout the last century have used this approach to study IOP, its disadvantages are clear. Cannulation of eyes is necessary to measure IOP with a water column manometer. This requires the complete immobility of the research subject, either by restraint or anesthesia. While several studies have yielded useful information with this approach, it places severe limits on the range of possible studies. For example, a study to characterize the normal diurnal cycle of certain common laboratory animals would be plagued with error using such an approach. The stress of restraint can cause elevations in blood pressure, leading to an artificially elevated IOP. Anesthesia and unconsciousness have long been known to cause a lowering of IOP in healthy eyes. The use of anesthesia would alter the normal diurnal cycle of the subjects, making any results obtained

highly questionable. These sources of error are not easy to characterize and control as physiological responses to stress and anesthesia vary among healthy living beings. A better course of action is to eliminate the need for anesthesia, handling, and restraint for the collection of IOP measurements. This can be done by collecting IOP data wirelessly using implanted sensors.

Among the many approaches to the challenge of wireless IOP measurement, the clearest distinction that can be drawn is related to the electronic complexity of these sensing systems. More specifically, where the complexity is located. Active and RFID devices have a high degree of complexity in the sensor itself, whereas the electronic complexity of passive sensing systems is located outside of the implant. Each approach comes with significant advantages and challenges. Many sensing applications for extreme environments use active systems. When direct measurements are needed in space, at the bottom of the ocean or deep underground, it makes sense to process and store data close to the sensing element, then deal with the problem of telemetry separately. Very low bandwidth telemetry are used in the latter two examples, techniques that are not capable of transmitting all the data these sensors collect in real time. In these cases, data must be processed locally so that when these sensors are interrogated they can provide brief, easy to communicate answers. To accomplish this, much more must be considered than simply the design of the sensor itself. Not only should a sensor element and antenna be designed to operate in these environments but all of the electronics associated with data processing, storage and telemetry. This approach can be very expensive and the added complexity of these systems introduce new possibilities for total failure of the sensing platform. But, for certain applications, no other approach has been devised. That is not the case for wireless biomedical monitoring. A passive sensor can provide real time data to an external unit

where it can be processed and stored. While the complexity of these external systems may be high, there are no constraints on its size or ruggedness to harsh biomedical environments. For these reasons, passive sensor are inherently lower cost and are capable of higher reliability. They can be fabricated from biocompatible materials that will not harm, or be harmed by the biomedical environment.

Active, RFID, and absolute passive sensors each have important roles to play in wireless sensing, including biomedical wireless sensing. The method chosen should depend on the application. It is the belief of the author that the approach of absolute passive sensing is best suited to wireless IOP monitoring because it is simpler, cheaper, and without the need to rely on the seamless operation of complex integrated electronics, has the potential to be the more reliable than active of RFID sensors.

CHAPTER 3: DESIGN AND SIMULATION

No active elements were included in the sensing and telemetry elements of the implanted device for reasons that have already been discussed. The passive wireless pressure sensor presented in this thesis is an inductor-capacitor (LC) circuit. The discussion in this section is divided broadly into the concepts of inductance and capacitance, and the principle of resonance that links them together. The sensing element in this device is a variable capacitor (Figure 3-1). Pressure acts on two parallel metal surfaces to push them closer together, causing an increase in capacitance. Pressure is read wirelessly by determining the resonant frequency shift associated with the shift in capacitance due to pressure. Telemetry is performed by inductive coupling, wherein energy is shared between a reader inductor and the integrated MEMS coil of the sensor though magnetic fields oriented axially to both. The characteristics of the signal generating this shared energy at the reader coil can be analyzed to determine the resonant frequency of the sensor. The inductance of the sensor and reader coils do not vary with pressure. The mutual inductance shared between them varies with distance and can influence the wirelessly-read sensor resonant frequency. This potential source of error can be minimized as discussed in section 3.3. This chapter will be organized as follows: A discussion on sensor design will include sensor capacitance, coil inductance and parasitic effects. Also included in this section will be an analysis of coil resistance, quality factor and inductive coupling efficiency. Section 3.2 is about the interaction of these concepts through the principle of resonance. Section 3.3 is an explanation of the phase dip telemetry technique.

The design and simulation goals discussed in this section are to maximize sensitivity and telemetry distance while minimizing size, complexity and cost. More specific design details are

specific to each version of the sensor and are discussed in chapters 4 and 5. It should be noted that apparent telemetry distance and sensitivity can be improved greatly with highly sophisticated and expensive readout equipment. It was determined that a sensitivity and impedance phase dip magnitude of at least 100 kHz/mmHg and 0.5° respectively are suitable for the practical implementation of this sensor. However, greater sensitivity and telemetry distance would further reduce the cost and complexity of an appropriate readout unit and should therefore continually pursued with each iteration of the sensor. The version I and II pressure sensors discussed in chapters 4 and 5 were designed for operation within the frequency range and measurement capabilities of the HP4191A Impedance Analyzer. This system is capable of measuring complex impedances in the frequency range of 100 kHz to 1 GHz with a minimum step of 100 kHz.

3.1 Sensor Design

The chosen telemetry method for this sensor is the impedance phase dip technique. This approach calls for weak inductive coupling between the sensor and reader coils. Weak coupling can be achieved by extending the distance between the coils, and therefore maximizing the sensing distance. By designing for the strongest possible coupling efficiency it is possible to achieve the greatest possible telemetry distance. Aside from coil separation, coupling efficiency depends heavily on the quality factor of the sensor. The quality factor is the ratio of energy stored in the inductor to the energy lost due to resistance of the sensor. A sensor with a sufficiently large quality factor could be wirelessly interrogated at very large distances, regardless of the dimensions of the sensor. However, the impedance phase dip becomes very

narrow with a very high sensor quality factor. The ability to detect a very narrow dip would require a very small frequency step as a readout unit scans the operating range of the sensor. Size and material limitations and the absolute-passive configuration of the sensor restrict the sensor quality factor to a value far below the point where this would have an appreciable effect.

Therefore, the sensor is designed to maximize quality factor by maximizing inductance and minimizing resistance. The capacitive sensing mechanism is designed to achieve the largest possible change in capacitance due to a pressure change in the range of interest.

3.1.1 Capacitance

Parallel-plate capacitance, illustrated in figure 3-1, is represented by the following equation: $C = \frac{\epsilon_r \epsilon_0 A}{d}$.

The quantity ϵ_r is the relative permittivity of the material between the capacitor plates, ϵ_0 is a constant representing the permittivity of free space, A is the overlapping area of the plates and d is the distance between them. In this capacitive sensing scheme, d, and effectively, ϵ_r , vary with

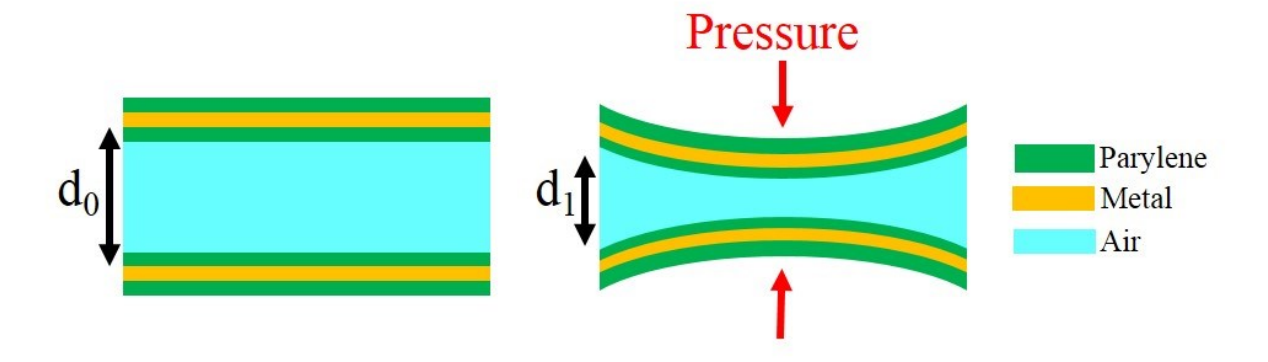


Figure 3- 1. MEMS capacitive pressure sensing element

pressure. An increase in pressure relative to the sealed pressure chamber causes an inward deformation of the capacitor plates, leading to an increase in capacitance.

This design calls for all metal layers to be encapsulated in Parylene-C. The relative permittivity of Parylene-C varies with frequency but is close to 3 in the operating range of this sensor. The relativity permittivity of air is slightly greater than 1. This system can be modeled as three capacitors in series, only one of which is variable. This configuration is illustrated in Figure 3-2.



Figure 3-2. Effective dielectric constant for multiple dielectric layers

The capacitances associated with each Parylene layer are equal, fixed and relatively large. In this figure, proportions are distorted for clarity. Note that Figure 3-2 is a 2-dimensional cross-section of 3-dimensional structure. The thickness of each Parylene layer is 5 μ m and the zero pressure air gap thickness is 60 μ m. The overlapping area, A, which includes a dimension into the page, is equal for the three capacitances. The capacitances associated with each Parylene layer inside the capacitor plates and the air gap between the plates are:

$$C_1 = \frac{\epsilon_1 \epsilon_0 A}{5 \ \mu m} = \frac{3\epsilon_0 A}{5 \ \mu m} \text{ and } C_0 = \frac{\epsilon_0 A}{60 \ \mu m}$$

The series combination of these capacitances is:

$$C_{eq} = \left(\frac{1}{C_1} + \frac{1}{C_0} + \frac{1}{C_1}\right)^{-1} = \left(\frac{10 \ \mu m}{3\epsilon_0 A} + \frac{60 \ \mu m}{\epsilon_0 A}\right)^{-1} = \frac{3\epsilon_0 A}{190 \ \mu m}$$

The effective dielectric constant between these capacitor plates is then determined by

$$C_{eq} = \frac{3\epsilon_0 A}{190 \ \mu m} = \frac{\epsilon_r \epsilon_0 A}{70 \ \mu m}$$

$$\varepsilon_{\rm r} = \frac{(70)(3)}{(190)} = 1.105$$

At a pressure of 100 mmHg, the average air gap is only 37.8 μm and the effective dielectric constant is:

$$\varepsilon_{\rm r} = \frac{(47.8)(3)}{(123.4)} = 1.162$$

Over the range of interest, from 0 to 100 mmHg, this effect results in a 5.14% change in capacitance due to the effective dielectric constant changing with pressure. The effective dielectric constant between the capacitor plates can be expressed as a function of plate separation as:

$$\varepsilon_{\mathbf{r}}(\mathbf{d}) = \frac{3(\mathbf{d} + 10)}{3\mathbf{d} + 10}$$

Where d, in units of μm , is the spacing between the two Parylene layers that coat the inner surfaces of the capacitor plates. This equation assumes these Parylene layers are each 5 μm thick with dielectric constant 3. The dielectric constant of air is assumed to be 1 in this equation.

The Parylene coating in the capacitive sensing chamber actually improves the sensing performance of the device versus a capacitive sensor with dielectric cavity of the same dimension filled only with air.

These equations and figures provide approximations for the zero pressure capacitance of the sensing element and help illustrate its operation. In practice, finite element simulation is better suited in the design and characterization of such a sensor. The Electromechanics Module of COMSOL Multiphysics FEM software was used in the design and characterization of the sensing element.

3.1.2 Inductive Coupling

The inductance determines in part the range of frequencies the sensor will resonate. To achieve a large telemetry distance high inductance is desired. This can be achieved by increasing the number of turns of the inductor. The inductance of a single turn coil of a particular dimension is given by:

$$L_0 = 2\pi d \left(10^{-7}\right) \left[log \left(\frac{4d}{w}\right) \left(1 + \frac{w^2}{24d^2}\right) - 0.5 + \frac{43w^2}{288d^2} \right] H$$

Where d and w are the average diameter and rim width of the single-turn inductor (Figure 3-3).

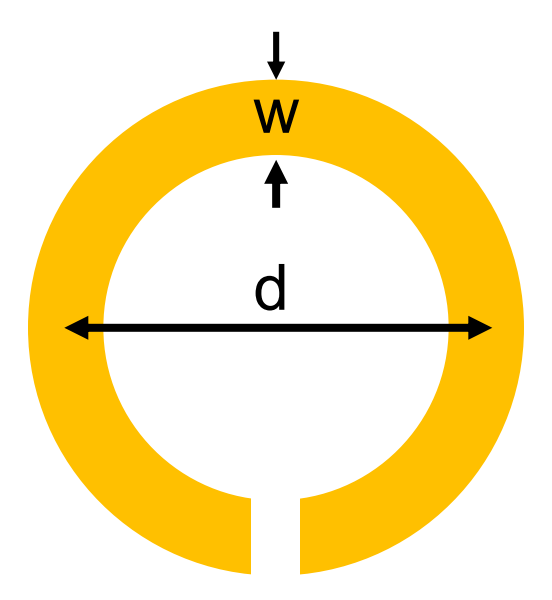


Figure 3- 3. Single-turn inductor

The self-inductance of multiple turn coils can be found by calculating the average turn diameter and width of all turns in the inductor then multiplying by the square of the number of turns, n.

$$L = n^2 L_0$$

The trade-off in adding more turns to a planar inductor given size constraints is that the resistance of the coil also increases with each turn added.

3.1.3 Resistance, Quality Factor and Coupling Efficiency

Resistance was determined to be a very important factor in the design of the integrated MEMS inductor in this device. The purpose of the inductor is to provide a telemetric link with

the reader coil at the greatest possible distance. The sensing distance depends on the ratio of coil resistance to inductance, called the quality factor of the inductor, Q.

$$Q = \frac{\omega L}{R}$$

Where $\omega = 2\pi f$ is the frequency at which the inductor Q is evaluated.

While inductance increases with the square of the number of turns added, resistance increases slightly more with each turn added. For example, a two turn inductor has a self-inductance of $4L_0$. The coil length roughly doubles in size and shrinks to about half its original width causing a resistance of about $4R_0$. The value would be exactly $4R_0$ if not for the nonzero separation needed between turns. A 5-turn planar inductor occupying a 2 mm rim width with a practical separation between turns of $50~\mu m$ would have a resistance 27.78 times greater than a single turn inductor of the same dimension. This comes from a 5 times resistance increase due to the 5 times coil length increase, and a 5(2/1.8) = 5.56 times increase due to the decreased width of each turn, including an allowance for the gap between turns, for a total of 27.78 times the resistance of a single turn coil of the same dimension.

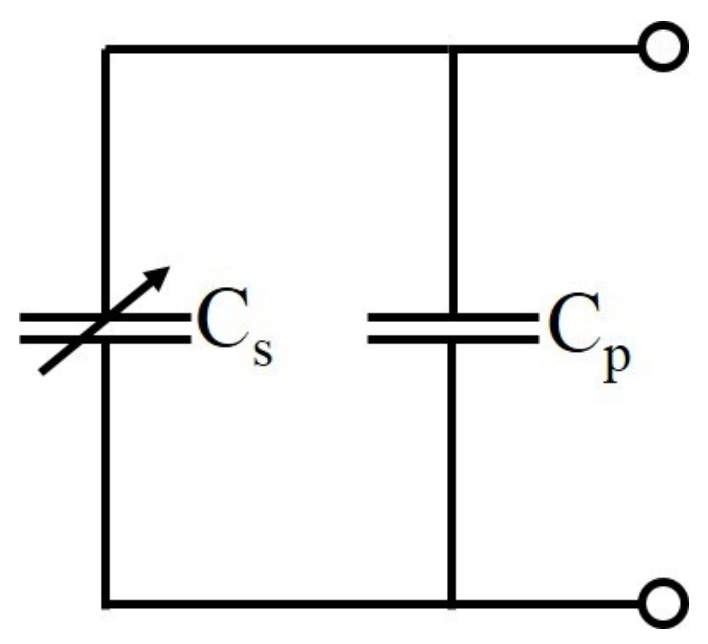


Figure 3- 4. Equivalent circuit for overall sensor capacitance

It was decided that inductors should be designed for very low resistances but still be able to operate in both air and liquid environments at frequencies below 1 GHz. The number of turns selected for each design has a large effect on the overall sensor frequency range of operation. Selection of an appropriate number of turns must then depend on other factors that contribute to the resonant frequency, notably parasitic capacitances.

3.1.4 Parasitic Effects

Every sensor design in this research makes use of only one metal deposition. Outside of the sensing element, where capacitance is desired, there are metal patterns in proximity to each other that will exhibit some capacitance. These are called parasitic capacitances. In a lumped circuit model of this sensor, parasitic capacitance is in parallel to the capacitive sensor (Figure 3-

4). The capacitance from a parallel combination of two capacitors is the sum of their capacitances: $C_{eq} = C_S + C_p$.

Parasitic capacitances have a negative effect on sensor performance. The resonant frequency of the device depends on the fixed inductance of the coil and the total capacitance of the sensor. Ideally, all capacitance in the device would be associated with the sensing element. Parasitic capacitances add to the total capacitance but do not vary with pressure. This means that a change in the sensor element capacitance is actually smaller change in the total sensor capacitance.

Two sources of parasitic capacitances in the sensor are from the bridge connecting the sensing capacitor and a distributed capacitance between turns of the inductor. These effects can be calculated analytically using the equations below:

$$C_{p} = \frac{(n-1) \times \pi \times d \times t \times \epsilon_{parylene} \times \epsilon_{0}}{1} + \frac{(n-1) \times 1.1 \times \epsilon_{0} \times A_{bridge}}{h}$$

The first term is the distributed capacitance between turns of the inductor. The overlapping area in this case is the total length of parallel metal traces, $(n-1)\times\pi\times d$ multiplied by the thickness of deposited conductor, t. Here, d is the average diameter of all inductor turns and l is the separation distance between adjacent turns. The second term represents the parasitic capacitance associated with the air bridge. The value 1.1 is an approximation of the dielectric constant that was discussed previously in this chapter. $(n-1)\times A_{\text{bridge}}$ is the area of overlap between the air bridge and every inductor turn it crosses. The denominator, h, is the height of the air bridge and is the same height as the capacitor chamber for these designs.

The above equations are a reasonable approximation of parasitic capacitance for the sensor in air. When it is placed in a higher dielectric medium, the parasitic effects increase

greatly. The electric field between two conductors will bend toward areas of higher dielectric constant. Capacitance due to electric fields outside the overlapping plane of the conductors is called fringe capacitance. When a high permittivity dielectric is placed between the capacitor plates, these fields are negligible by comparison. In the case of this sensor, the dielectric constant of the material surrounding the sensor is higher than the dielectric constant between capacitor plates so fringe capacitance cannot be ignored. Figure 3-5 is a two dimensional cross section of a typical two-turn sensor coil.

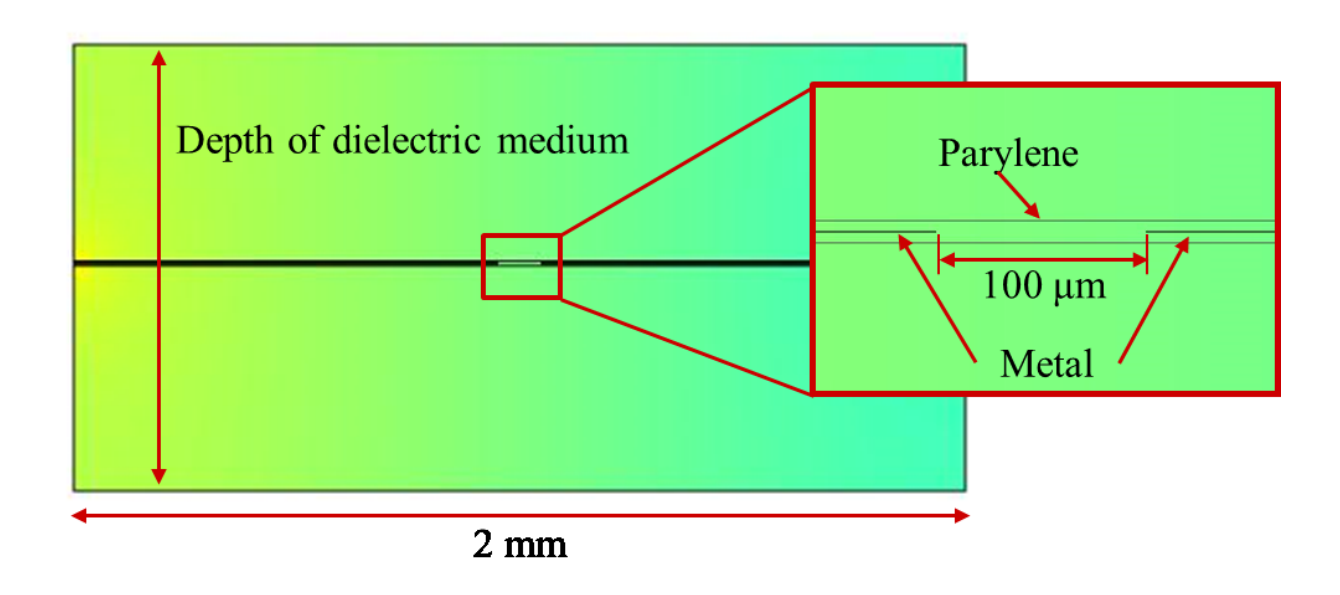


Figure 3- 5. Cross-Section of a two-turn coil used for COMSOL simulation

The thickness of metal in this simulation is 500 nm and is encapsulated in a 5 μ m thick Parylene coating. The Parylene thickness in the area between metal traces is 10 μ m. The dimension into the page for this simulation was specified as the total length of the gap between turns, 12π mm, in this case. Simulations in COMSOL Multiphysics were conducted for both air and water media to gauge their effect on coil parasitic capacitance. The depth of the media was varied in the range

of 0 to 8 mm. Figure 3-6 is a plot of coil parasitic capacitance versus the depth of the medium in which the coil is measured.

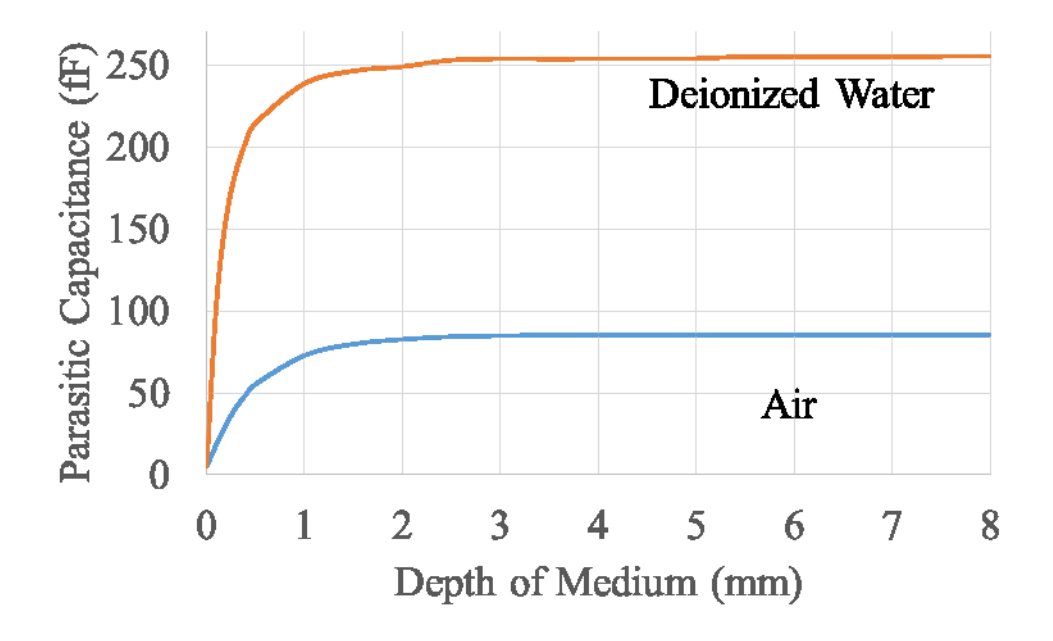


Figure 3- 6. Coil parasitic capacitance versus depth of dielectric medium

These plots stabilize above about a depth of about 6 mm. The capacitance difference from 6 mm to 8 mm for air and water are 0.007% and 0.009% respectively.

The bridge connecting the two capacitor plates together is 400 μ m in width and overlaps a single turn of the underlying coil with a width in this vicinity of 400 μ m. The distance between these overlapping areas in the same as the chamber height for this sensor, 70 μ m. The bridge parasitic capacitance was calculated as:

$$\frac{1.1 \times \epsilon_0 \times (400 \mu m)^2}{70 \mu m}$$
 =22.3 fF

for the air medium, where the area and height of the bridge are $(400 \ \mu m)^2$ and $100 \ \mu m$ respectively. In the case of a water medium, bridge capacitance were calculated as:

$$C_{eq} = \left(\frac{10 \ \mu m}{3 \varepsilon_0 A} + \frac{60 \ \mu m}{10 \varepsilon_0 A}\right)^{-1} = \frac{3 \varepsilon_0 A}{28 \ \mu m} = 152 \ fF$$

Table 1 summarizes the inductive and capacitive properties of this sensor and shows the effect they have on its resonant frequency.

Table 3-1. Effect of dielectric medium on sensor response

	No Medium	6+ mm Air	6+ mm Deionized Water
Coil Parasitic	5.05	85.5	255
Capacitance (fF)			
Air Bridge Parasitic	0	22.3	152
Capacitance (fF)			
Sensing Capacitance (fF)	244	244	244
Total Capacitance (fF)	249.05	352	651
Coil Inductance (nH)	113	113	113
Sensor Zero-Pressure	948.72 MHz	799.15 MHz	586.8 MHz
Resonant Frequency			

3.2 RLC Resonance

So far, each component that contributes to the sensor's resonant frequency and quality factor have been discussed. An equivalent circuit model for the complete sensor is shown below in Figure 3-7.

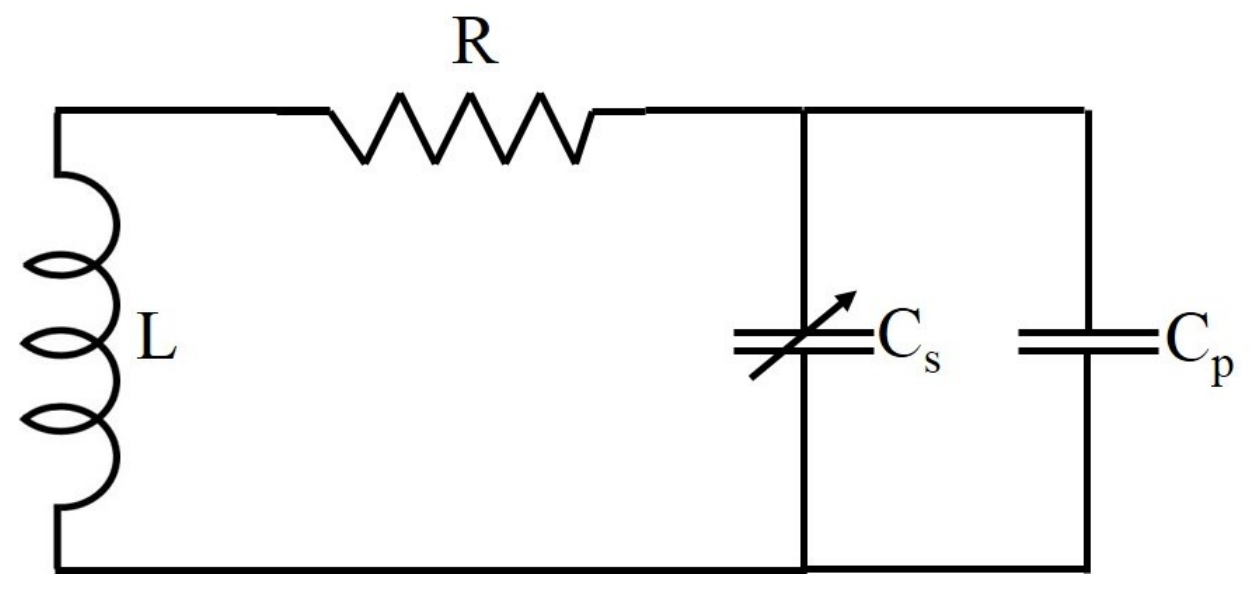


Figure 3-7. Equivalent circuit for the sensor

This is a series RLC circuit with complex impedance:

$$Z_{eq} = R + j \left(\omega L - \frac{1}{\omega (C_S + C_P)} \right)$$

The resonant frequency occurs at the frequency, ω , where the total impedance is purely real. It is found by setting $\omega L - \frac{1}{\omega C} = 0$. Solving for ω yields

$$\omega_0 = \frac{1}{\sqrt{L(C_S + C_P)}}$$

To find the resonant frequency in Hertz, ω_0 =2 πf_0 is substituted, giving

$$f_0 = \frac{1}{2\pi\sqrt{L(C_S + C_P)}}$$

At this frequency, currents entering the circuit are at their maximum magnitude. Currents are induced in this sensor by a time-varying magnetic field caused by a reader coil held coaxial and in close proximity to its integrated planar MEMS coil.

3.3 Impedance Phase Dip Technique

When two inductors are held in close proximity and time-varying current is passed through one, a magnetic field is created that induces a current in the other. The degree to which a current may be induced in a coil is called coupling efficiency. High coupling efficiencies, close to 1, are possible with low frequency signals and often require high magnetic permeability materials between coupled coils. In this application, we try to achieve weak coupling in order to obtain accurate and repeatable readings of the sensor resonant frequency. Figure 3-8 shows an equivalent circuit for the sensor inductively coupled to an external reader coil.

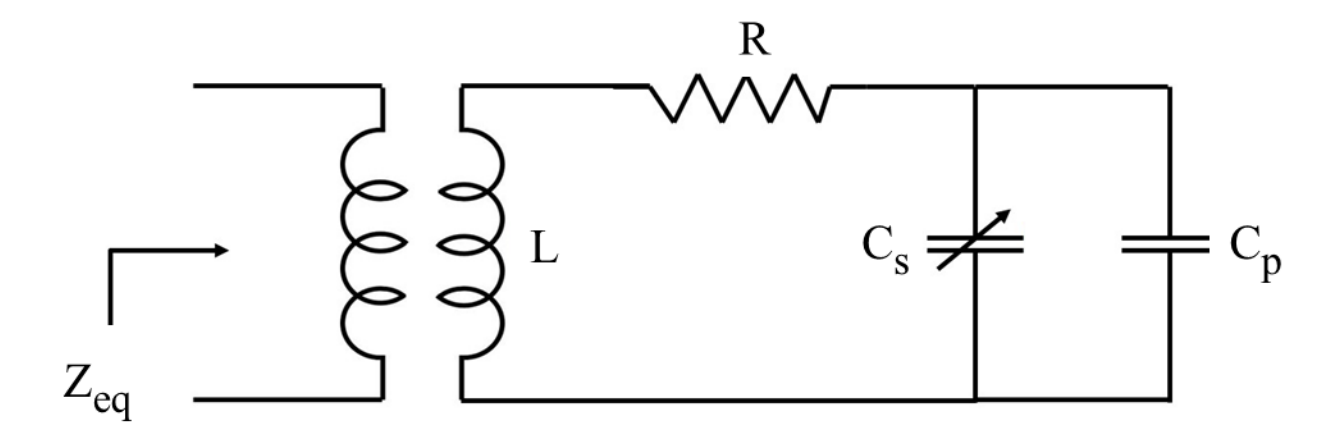


Figure 3- 8. Inductive coupling between reader and sensor coils for phase dip telemetry

The complex impedance of the reader coil is read at its terminals for a range of frequencies. If perfect coupling efficiency was achieved with this configuration, the measured impedance phase would shift abruptly at the sensor resonant frequency from 90°, which indicates an inductive equivalent circuit, to -90°, indicating a capacitive circuit, crossing 0° precisely at the resonant frequency of the sensor. With very weak coupling a small dip in the measured impedance phase would be observed very near the resonant frequency of the sensor. The location of this dip approaches the true resonant frequency of the sensor as coupling efficiency decreases. The impedance phase dip technique is an approximation, but a very precise one with low coupling efficiency. Figure 3-8 illustrates the importance of weak coupling when using the impedance phase dip technique.

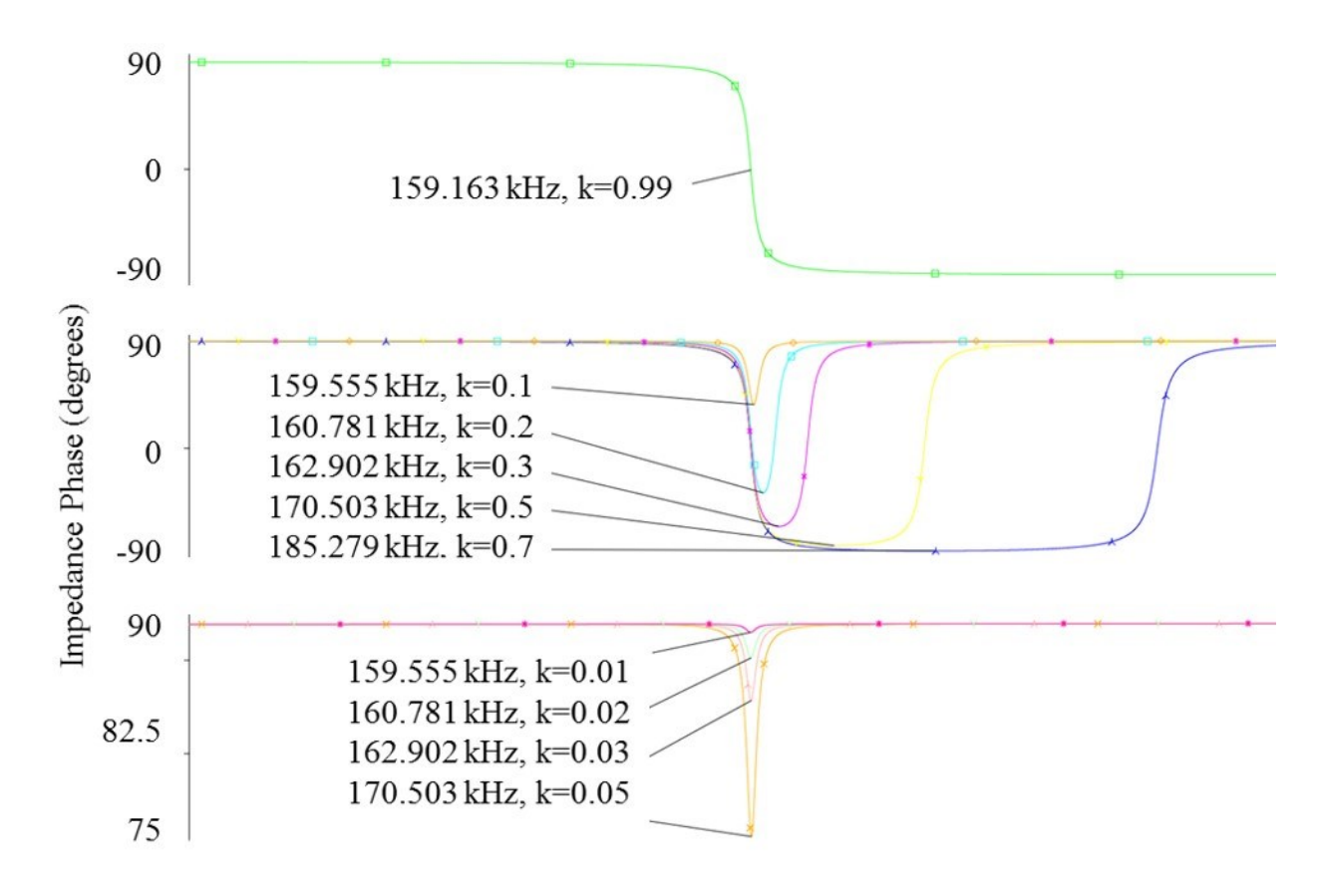


Figure 3- 9. PSPICE simulation illustrates the importance of weak inductive coupling

The true resonant frequency of this circuit is displayed in the top window of this figure. As can be seen from the bottom window, only a coupling efficiency of 0.01 yielded six digits of precision in this simulation. For practical purposes, such high precision is rarely required. Coupling efficiencies above 0.1 begin to shift the phase dip minimum significantly. As coupling efficiency increases, the phase dip widens and its minimum moves to higher frequencies.

3.4 Conclusion

This chapter discussed the factors that were considered in the design of the wireless IOP sensors that will be presented in Chapters 4 and 5. A detailed analysis of the sensor elements was presented and an equivalent circuit for the overall sensor was developed and analyzed. This chapter provided a review of the concept of RLC resonance and the impedance phase dip technique to wirelessly measure sensor resonance. The fabrication processes for these sensors also play an important role in their design due to restrictions placed on materials, size and cost. These processes are presented in detail in Appendices A and B.

CHAPTER 4: VERSION I SENSOR

This chapter describes the design, fabrication, and characterization of a wireless, flexible, passive pressure sensor. The integrated planar MEMS coil and the variable capacitor were constructed using a fold-and-bond technique, which avoids multilayer processes and thus reduces fabrication complications. Parylene-C was the structural and packaging material, which ensures the flexibility and biocompatibility of the sensor.

This chapter will be divided into four parts. First, the goal of this research will be presented briefly with an emphasis on the specific problems this device sought to overcome.

Next, the sensor design and fabrication will be discussed. Section 4.3 will include testing procedures and results. Finally, a detailed analysis of the achievements and shortcomings of the version 1 sensor will be presented.

4.1 Design Goals

The overall goal of this research is to design a wireless implantable pressure sensor that is suitable for 1-2 year large-scale glaucoma studies involving research animals. An acceptable design would be capable of providing 1 mmHg pressure sensing resolution at a telemetry distance of at least 20 mm. It would be fabricated entirely from biocompatible materials at a cost that would not be prohibitive for a research budget. The surgical procedure to implant the device should be minimally invasive, simple and quick. This requires the sensor to be rugged, and either very small or very flexible. For a passive design using impedance phase dip telemetry, size is of great importance. A large device is necessary to provide the inductive link necessary to obtain

readings at a comfortable distance. The version 1 sensor succeeded in meeting some objectives but fell short for others. The design specifications and performance objectives for this sensor are listed in Table 4-1.

Table 4- 1. Design specifications for the version I sensor

Overall dimensions	Flat, thin and round	
	Outer diameter ≤ 16 mm	
	Hole in center ≥ 8 mm in diameter	
Materials	All Biocompatible	
	Flexible	
Fabrication	Simple, low cost	
	Single metal deposition	
Performance	Telemetry distance ≥ 20 mm in isotonic saline	
	Operation within 100 kHz – 1 GHz range	
	Sensitivity ≥ 100 kHz/mmHg in water	

4.2 Design and Fabrication

The implantable consists of a three-turn planar inductor, the terminations of which are folded into a flexible parallel-plate capacitor supported by rigid SU-8 sidewalls. Sealing the plates in this configuration forms a chamber with volume that is dependent on the rigidity of its components and, importantly, the pressure of the environment where it is implanted. The change in chamber volume is facilitated by deflection of the flexible capacitor plates. These deflections cause a change in the sensor capacitance, which shifts the resonant frequency of the LC sensor system. As pressure increases, the resonant frequency of the sensor is shifted to a lower value.

As discussed in Chapter 3, the key to maximizing telemetry distance for this sensor is minimizing its coil resistance. Another factor that was considered in this design is the frequency range over which a single turn reader coil would exhibit an inductive impedance. While inductive coupling still occurs between the reader and sensor beyond the self-resonant frequency of the reader coil, the degree to which inductive coupling occurs is reduced. This results in a lower measured phase dip for a given coil separation and therefore a lower telemetry distance. Although a two-turn configuration for this device would exhibit a greater quality factor due to lower resistance, a three-turn configuration was chosen to ensure the sensor would resonate in air at the frequency range for which the reader coil has an inductive impedance. The entire available rim width of 4 mm was used in the construction of the coil to minimize its resistance. The gap between adjacent turns is 100 µm. The pressure sensing element is elliptical in shape and exhibits a capacitance of 1.22 pF with a plate separation of 60 µm at atmospheric pressure.

Only four materials were used in the fabrication of this sensor, including a small strip of adhesive tape. Parylene was used to package the metal layer of the sensor. SU-8 provides a rigid support for the capacitive sensing chamber and pressure reservoir. Bonding was performed with a piece of thin adhesive tape placed along the perimeter of the pressure reservoir. To ensure a good seal and to improve biocompatibility a small amount of PDMS was coated along this bonding interface. When placed under a slight vacuum, the formation of small bubbles was noted at the interface, indicating a possible leak. Before curing the PDMS, the sensor was removed from the vacuum chamber and returned to atmospheric pressure. This allowed some PDMS to enter the gaps in the interface and form a reliable seal. A detailed fabrication process for this sensor is given in Appendix A.

Fig. 4-1 shows a fabricated device before and after bonding. Several thin channels are fabricated in the SU-8 structure contacting each capacitor chamber. The channels on opposing plates are perpendicular.

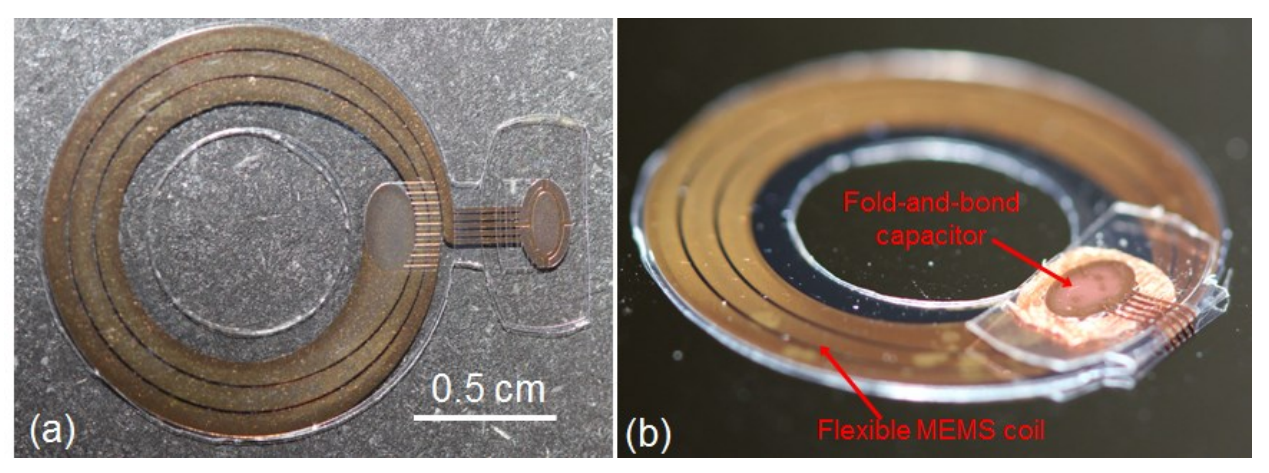


Figure 4- 1. Fabricated Sensor (a) before and (b) after bonding

When the device is bonded, these channels form a rigid cavity connected to the capacitor chamber and act as a pressure reservoir. Adding rigid volume to the capacitor chamber allows greater deflection of the capacitor plates under the same pressure conditions. The SU-8 layer along the coil provides a flat support to help maintain the shape of the sensor. After being flexed, the device always returns to its original shape. This was intended to aid in the implantation procedure in the eye, but for reasons discussed in Section 4.4.2, is not practical for that purpose. Theoretical sensor inductance and capacitance are listed in Table 2 along with predicted and measured values for the sensor resonant frequency. These values were obtained by calculation and simulation as described in Chapter 3.

Table 4-2. Theoretical and Measured Version 1 Sensor Characteristics

	Air	Deionized Water
Coil Parasitic Capacitance (fF)	171	510
Bridge Parasitic Capacitance (fF)	89.0	607
Sensing Capacitance (pF)	1.22	1.22
Total Capacitance (pF)	1.48	2.34
Coil Inductance (nH)	177	177
Theoretical Zero-Pressure Resonant Frequency	311 MHz	247 MHz
Measured Zero-Pressure Resonant Frequency	317 MHz	202 MHz

4.3 Testing Procedures and Results

The pressure sensor was tested in air, deionized water, and 0.9% saline solution. Pressure sensitivity tests were conducted in the range of 1 mmHg to 100 mmHg for air and deionized water. The testing setup used for a liquid environment is shown in Figure 4-2. The sensor is secured in a plastic testing chamber (b) that is suspended above a single turn reader coil. The impedance phase of the reader coil is measured by an HP 4191A impedance analyzer (d). The syringe pump (a) injects liquid into the test chamber in increments of one inch. Once the four-inch chamber is filled, the water column is raised another 48 inches in (c) and measurements are taken every inch. Each inch of water corresponds to 1.87 mmHg. Pressure sensitivity measurement in all media took place at a telemetry distance of 15 mm.

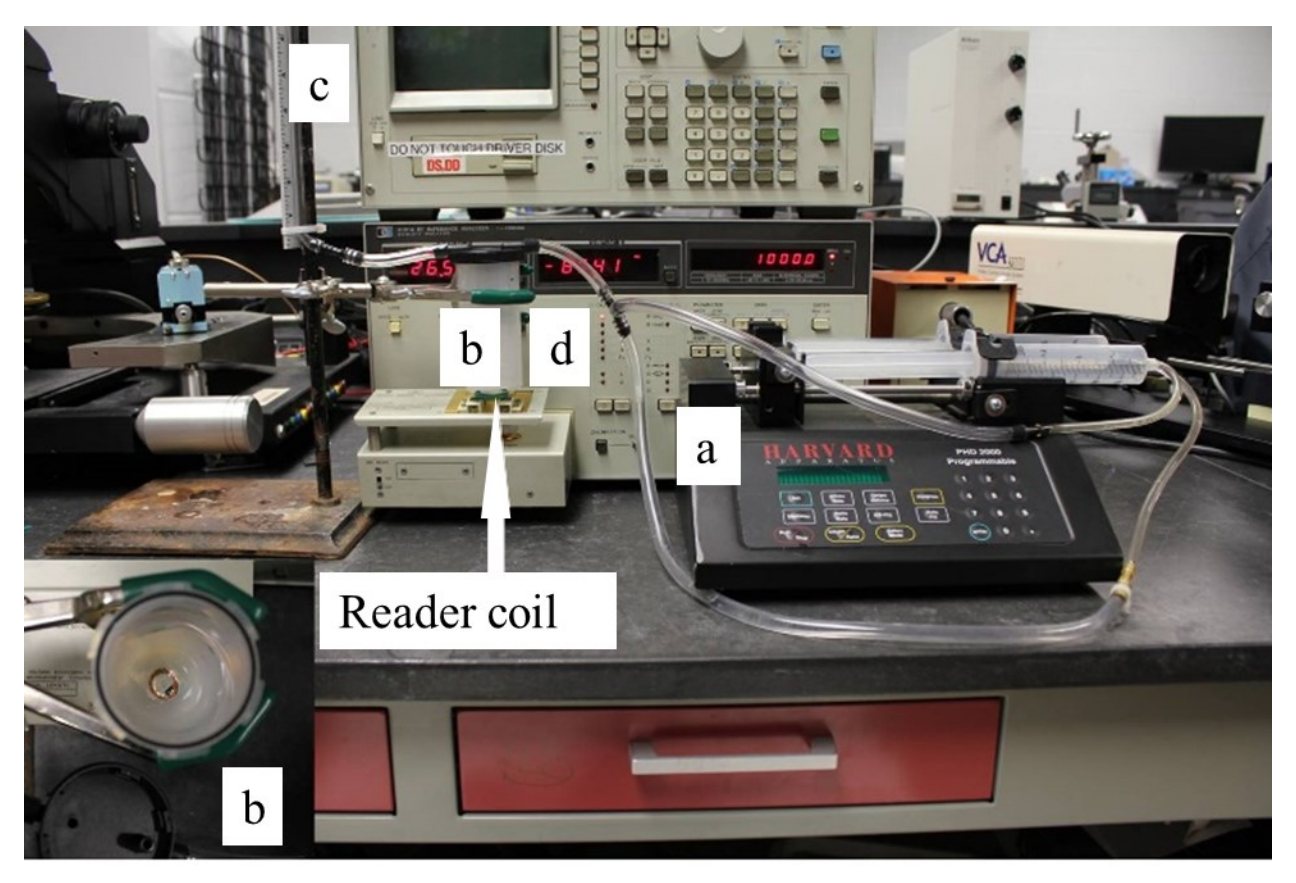


Figure 4-2. Water testing setup for version I sensor

Pressure testing results are plotted in Figure 4-3. The left plot indicates the frequency at which a minimum in the phase dip is noted for each pressure condition. Also shown are some typical impedance phase curves for several pressure conditions. As can be seen from the figure, the phase dip minimum occurs at lower frequencies for higher pressure conditions.

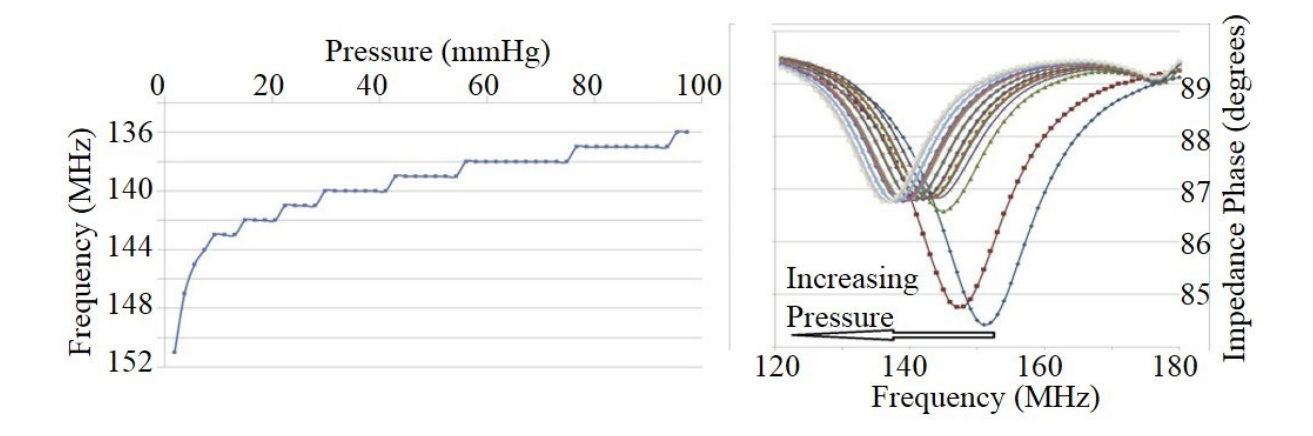


Figure 4- 3. Results of water pressure testing

The effect of different media on the sensor is also investigated with results summarized in Figure 4-4. For these tests the sensor is suspended on a glass slide 10 mm above the base of a glass beaker. For liquid testing the sensor is submerged to a depth of 2 cm. The beaker is suspended 5 mm above the reader coil. There is a large drop in the sensor resonant frequency when it is placed in deionized water. Water has a dielectric constant 10 times greater than air. The parasitic capacitance of the device varies proportionally with this higher dielectric constant. Saline is a lossy medium with a complex dielectric constant. This reduces the phase dip magnitude and the apparent quality factor of the sensor.

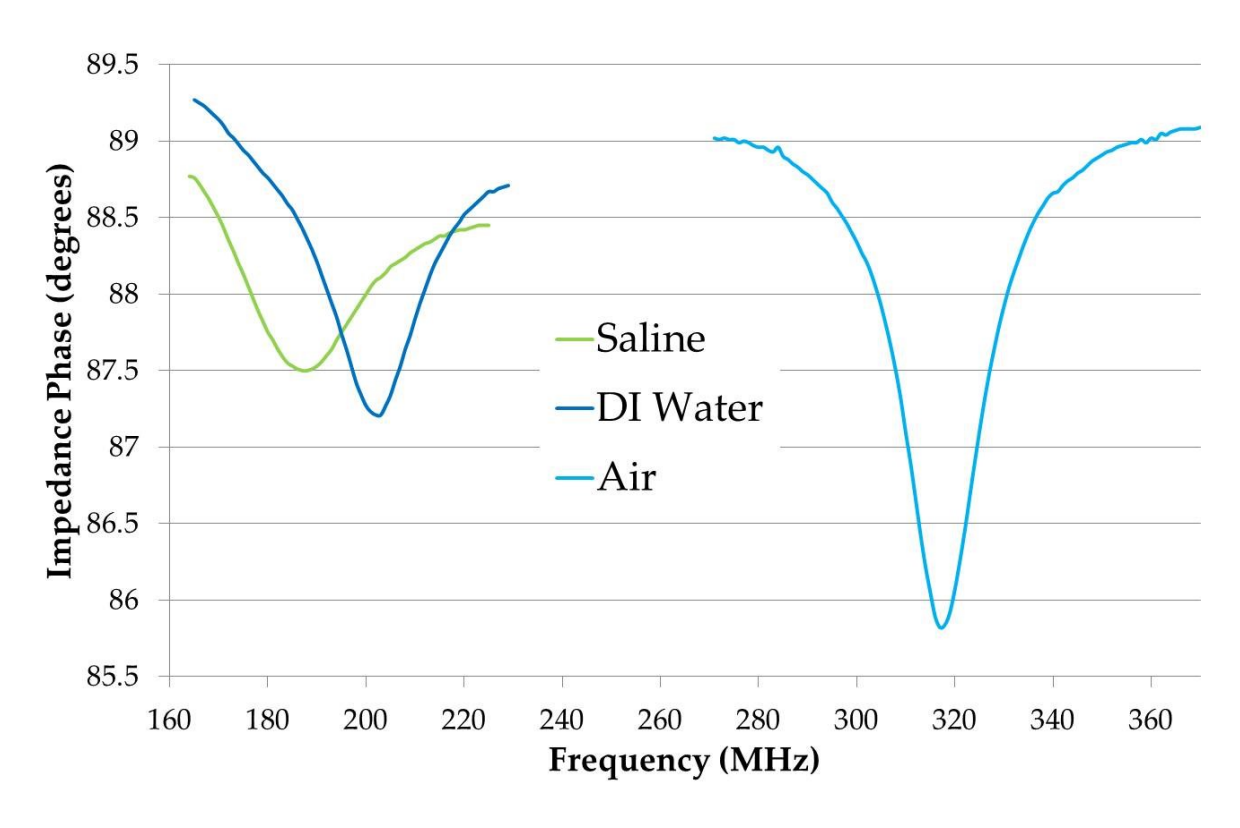


Figure 4- 4. Pressure sensor frequency response to different media

A summary of testing results is listed in Table 4-3 below. Average pressure responses are included as well as the maximum telemetry distance achieved in each medium. Maximum telemetry distance in this case is defined as the maximum distance where the impedance phase dip can be easily distinguished from measurement noise.

Table 4-3. Summary of results for version I sensor testing

Media	Air	Deionized Water	Saline (0.9%)
Pressure Sensitivity	140 kHz/mmHg	156 kHz/mmHg	N/A
Telemetry Range	35 mm	28 mm	15 mm

4.4 Remaining Challenges

This sensor met several of the minimum design goals and performance objective listed in Table 4-1 but a great deal of room for improvement still remains. This section will discuss the negative characteristics of this sensor as well as areas of acceptable performance that can be further improved.

4.4.1 Biocompatible Materials and Interface Sealing

The first major drawback of this sensor is the interface of the capacitive sensing chamber. While the seal made from a combination of adhesive tape and PDMS was effective, it is not practical for an IOP monitoring system. Even though the adhesive tape was encased in PDMS, the tape itself is not biocompatible. The purpose of using only biocompatible materials is to prevent damage to the eye, even in the event the device is damaged and underlying materials are exposed. Furthermore, any sealing interface that is exposed to the harsh intraocular environment is likely to degrade over time and become a source of failure for the device. High temperature annealing of interfaces in an inert environment could reduce the potential for failure. It was not possible in this case due to the location of the interface very near the fragile pressure sensing element.

4.4.2 Flexibility

The flexibility of this sensor should also be considered a shortcoming. The benefits of including the 30 µm SU-8 layer above the sensor coil have already been discussed but limits the device flexibility to an extent that would cause a high rate of complications during the implantation surgery. While the sensor can be bent 180° (Figure 8), it cannot be folded. Any attempt to do so will fracture the SU-8 layer, often tearing the underlying Parylene and metal. The handling necessary for minimally invasive implantation would cause the sensor to fracture. More invasive approaches such as making a very large incision in the cornea would be needed to implant the version 1 sensor. The purpose of making the device flexible is to enable both large sensor size and minimally invasive implantation. This sensor has apparently failed in that regard. Including an SU-8 layer only in the area surrounding the sensing chamber would certainly mitigate this problem.

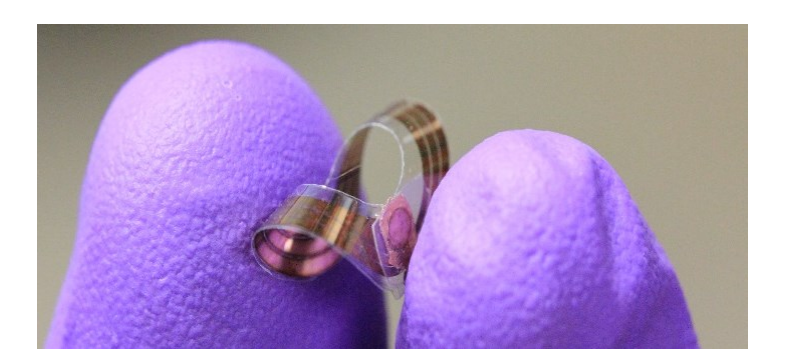


Figure 4- 5. Flexibility of the version I sensor

Still, the fragility of a small, thin SU-8 structure necessitates very delicate handling.

4.4.3 Performance

While this device met minimum telemetry and sensitivity performance objectives, there remains room for improvement in these areas. The inclusion of a third inductor turn increased coil resistance and parasitic capacitance. This reduced the sensor quality factor due to increased coil resistance and reduced sensitivity due to the increased non-pressure-sensitive capacitance. The pressure sensing element can be engineered to provide better sensitivity. Figure 4-3 shows that the highest sensitivity and linearity of this sensor occurs at a very low pressure range. Another fabrication strategy could allow greater capacitor plate deflection for the entire range of the sensor.

4.5 Conclusion

This chapter presented a wireless, flexible, passive pressure sensor that is a stepping stone towards enabling passive, long-term intraocular pressure monitoring. The coil size allows for large telemetry distances, even in lossy saline solutions. To demonstrate the sensing ability of the devices, fabricated pressure sensors were characterized in air, DI water, and saline environments. A pressure sensitivity of 156 kHz/mmHg and a maximum detectable range of 28 mm were achieved in DI water. The sensor can achieve telemetry through 10 mm of isotonic saline at an overall sensor-to-reader separation of 15 mm. This indicates a high likelihood that a sensor could achieve a practical telemetry distance when implanted in an eye, where the anterior chamber depth typically does not exceed 3.6 mm.

CHAPTER 5: VERSION II WIRELESS IOP SENSOR

This chapter describes a flexible, highly responsive wireless intraocular pressure sensor. As with the first iteration of this device, the sensor is comprised of an integrated planar MEMS coil and a variable capacitor. A novel fabrication process has enabled higher sensitivity and greater flexibility than previous iterations. This sensor was designed with an outer diameter and rim width of 14 mm and 2 mm, much smaller than the previous version at 16 mm and 4 mm. Still, this sensor exhibits an improved telemetry range and a vastly improved sensing performance.

This chapter will be organized as follows: First there will be a discussion of the unresolved challenges of the version 1 sensor and the solutions proposed in this new design.

Next, a complete overview of the version 2 sensor design will be presented. Section 5.3 will cover testing setup and results. Finally, a summary of the achievements of this sensor will be reported.

5.1 Version I Sensor Challenges and Solutions

The version 1 sensor proved that the techniques discussed for passive, wireless IOP sensing are feasible for animal studies in glaucoma research. All of the minimum performance requirements were met without straying from the design parameters regarding size and shape. However, it is not expected that the version 1 sensor would perform adequately after animal implantation for the entire course of a 1-2 year glaucoma study. Firstly, the capacitive pressure chamber interface is likely to fail. Second, the use of adhesive tape violates a design parameter.

Only biocompatible materials are to be used in this sensor. Third, the use of SU-8 in the version I device made it impossible to fold, and extremely fragile. Lastly, although the version I sensor met minimum performance requirements, better sensing and telemetry performance can be achieved.

5.1.1 Sealing of the Fold-and-Bond Interface

Any bonded interface of a device implanted in the harsh biomedical environment is a likely failure point. To overcome this challenge, the fold-and-bond interface was eliminated in the latest version of the sensor. In the version I sensor, the chamber walls were fabricated and, as a final fabrication step, bonded together. In this version, the chamber is created in a slightly different way. A thick layer of AZ4620 photoresist is patterned on top of Parylene encapsulated metal patterns. The top metal plate and the thick photoresist covering it are cut and folded out from the substrate. Under slight pressure the top photoresist is pressed against the bottom layer. At 95°C the photoresist begins to melt and after 5 minutes the interface between the top and bottom layers disappears. When the devices are eventually coated with Parylene, the sidewalls of the capacitor chamber are formed by coating directly on this photoresist. There is no interface in the vicinity of the capacitor chamber because it is entirely encapsulated in a single layer of Parylene. Figures 5-1 through 5-3 illustrate this process.



Figure 5- 1. Patterned photoresist



Figure 5- 2. Melting photoresist interface

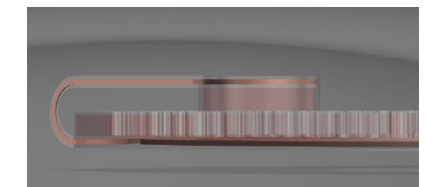
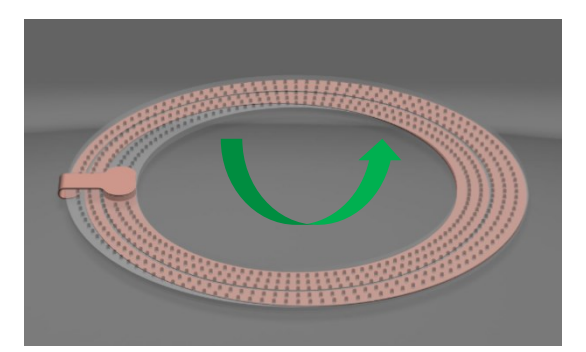


Figure 5- 3. Parylene coating

5.1.2 Flexibility

These pressure sensors need to be flexible enough to be rolled or folded into a small area suitable for implantation. There are four factors that were considered in designing this second sensor for flexibility: creasing, shape recovery, durability, and thickness. Parylene itself is very flexible and can be rolled or folded easily without damage. The same cannot be said about thin metal films. If a Parylene encapsulated metal film is folded, it will crease, immediately affecting the electrical properties of the sensor. Often, a crease causes the metal to break entirely. The SU-8 layer in the version 1 device, while intact, prevented creasing of the metal layer. This was of limited usefulness since the very fragile SU-8 layer tended to tear through metal and Parylene



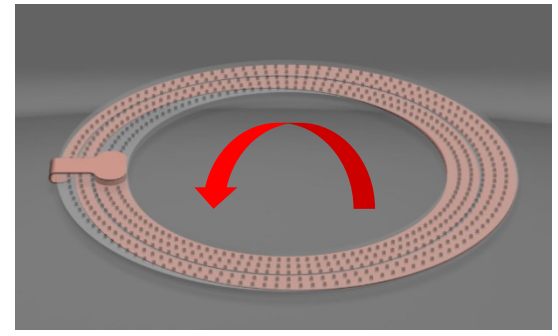


Figure 5-4. Resistance to creasing when folded in toward Parylene support structure

when fractured. The new design resists creasing when folded in toward the Parylene support structure (Figure 5-4). It can be folded flat on itself with light pressure. Creasing is still possible if heavy pressure is used when folding or if the sensor is folded away from the Parylene support structure.

These sensors tend to recover their shape several minutes after folding. To enable quicker shape recovery and eliminate the problem of creasing, the sensors can be coated in PDMS. Very thick coatings provide faster recover and higher durability but prevent folding into a very small shape. A very thin PDMS coating will slough away even with gentle handling. A device of total thickness $\sim 300~\mu m$ due to a PDMS coating is a reasonable middle ground. These devices can be folded on themselves in either direction and held firmly without damaging the PDMS surface or causing a crease in the metal layer.

5.1.3 Biocompatibility

Only Parylene, metal, and PDMS are included in the fabricated device. The metal used for prototype devices is copper, which is not biocompatible. Gold may also be used with a slight modification of the fabrication process and due to its malleability and corrosion resistance, should provide better overall sensor performance than copper.

5.1.4 Overall Sensor Performance

One simple way in which the version 1 sensor can be improved upon is by including only two turns in the integrated MEMS coil. It was discussed in Chapter 3 that reducing the number of

coils reduces resistance more than it reduces inductance. Decreasing the ratio of resistance to inductance increases the quality factor of the device and therefore its telemetry range. Reducing the number of turns also reduces parasitic capacitances between coil turns and at the bridge. Reducing parasitic capacitance increases the proportion of total sensor capacitance that varies with pressure, enabling greater changes in sensor resonant frequency with pressure.

The design of the pressure sensing element also plays a role in the increased sensitivity of this device. In the previous version, the greatest sensitivity was achieved for very low pressures. The rigid SU-8 sidewalls of the previous design prevented a very large deflection of the capacitive diaphragms above a certain pressure. The thin Parylene sidewalls of the new design are able to flex in response to pressure, enabling greater capacitor plate deflection.

Lastly, a better designed pressure reservoir allows for greater capacitor plate deflection. The relatively small pressure reservoir in the previous design makes it impossible for the sensing diaphragm to deflect near the level its mechanical properties would allow. The larger pressure reservoir in the new design spans the entire rim of the device. The greater air volume means a smaller volume change occurs with movements of the sensing diaphragm. Therefore less pressure must be exerted on the sensing element to achieve the same capacitance change as the version 1 sensor.

5.2 Sensor Design

As discussed previously, a fold-and-bond technique was employed prior to Parylene-C encapsulation to form the capacitive sensing chamber. The device consists of only three materials: Parylene-C as the primary structural and packaging material, a single metal layer, and

a small amount of PDMS to seal a Parylene-C pressure reservoir that spans the surface of the device. The inner and outer diameters of this device are 5 mm and 7 mm respectively. The thickness is 45 μ m, with an additional 30 μ m of thickness at the capacitive sensing element (Figure 5-4). A version of the device that has been encapsulated in PDMS has a total thickness of \sim 300 μ m. This PDMS layer makes rolling the device for implantation much easier and improves durability and recovery to a flat shape after rolling.

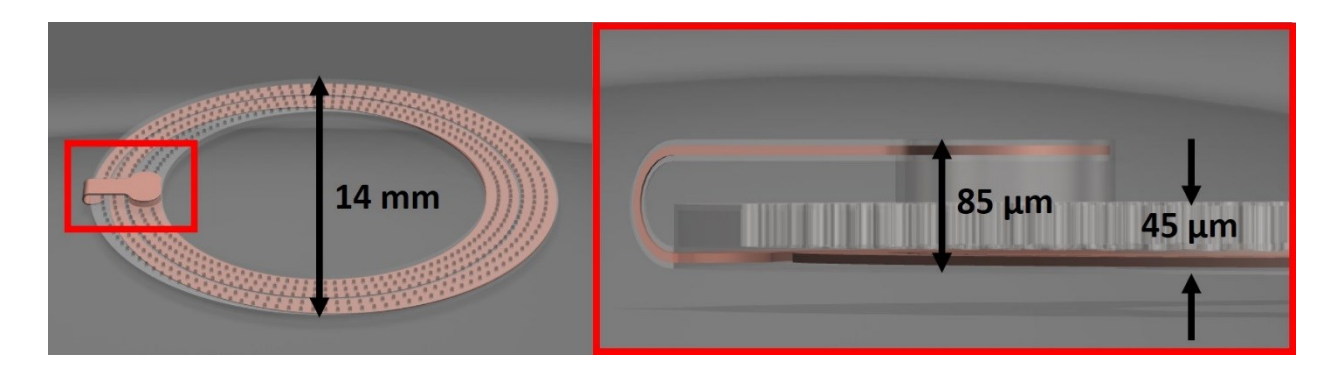


Figure 5- 5. Sensor dimensions

The rounded capacitor has a larger dimension of 2 mm and a smaller dimension of 1 mm. The thickness of the various layers in Figure 5-5 is exaggerated in these images for clarity. Only one metal deposition and three Parylene depositions are needed to fabricate this device. Two masks were used in the process: one to pattern metal and one to pattern the photoresist mold upon which the final Parylene deposition was made. A detailed fabrication process is included in Appendix B.

5.2.1 Sensor Properties

The inductance and sensor capacitance were found by simulation in the Magnetic and Electric Fields and Electromechanics modules of COMSOL Multiphysics. The parasitic capacitances and resonant frequency were calculated using the equations and simulation techniques described in Chapter 3. Table 5-1 is a summary of the sensor properties at atmospheric pressure.

The photolithography masks used for metal and photoresist patterning in all experiments are designed in Autocad. A portion of the 2-D mask used for metal was imported into COMSOL and extruded out of the plane by 500 nm. The capacitor plates at the terminations of this coil were removed and replaced with long connectors to reach the edge of an electrically and magnetically insulated box in which the sensor is contained. Results from the inductance simulation are presented in Figure 5-6 and Table 5-1.

The streamline plot of Figure 5-6 shows that the magnetic field lines are constrained by the magnetically insulated walls of the box. The magnetic fields field strength at these walls is several orders of magnitude lower than the field strength closer to the sensor. This indicates the box is of adequate size to obtain useful inductance values from this simulation. In this figure the magnetic field strength is represented by color in the streamlines. Very close to the inductor portions of the streamlines are red. The color shifts to dark blue further from the inductor at the box edge.

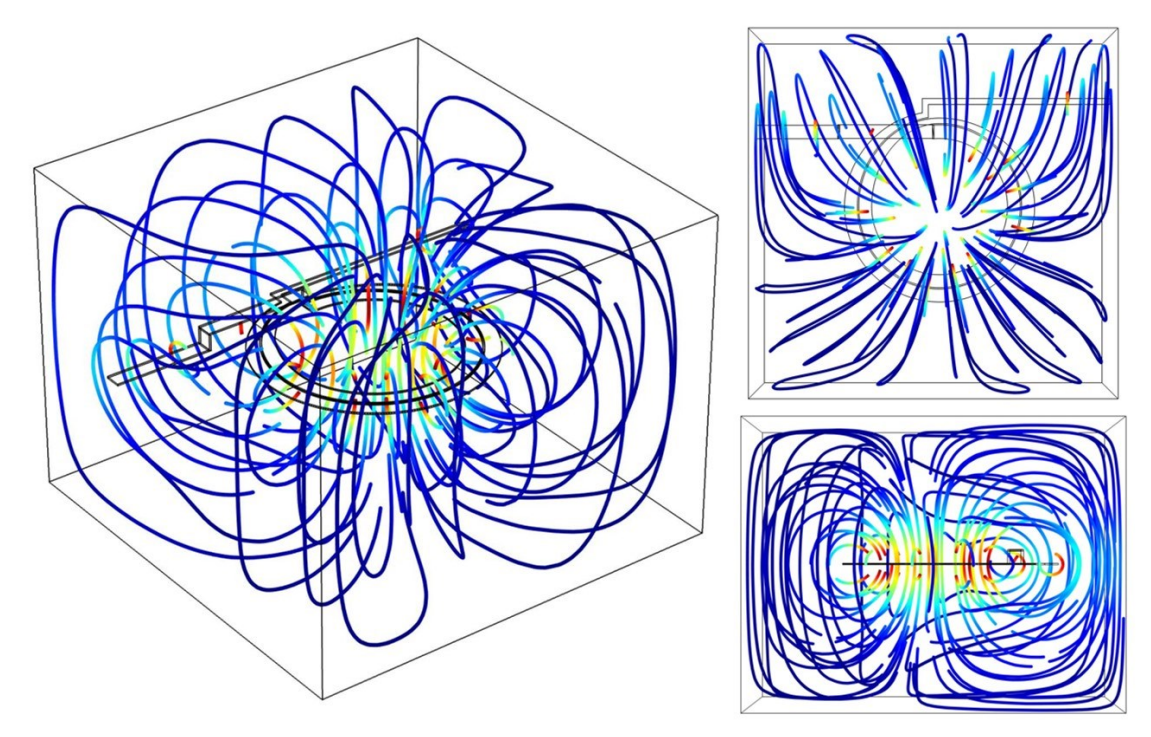


Figure 5- 6. COMSOL simulation of inductor magnetic field

Table 5-1. Theoretical sensor characteristics

	Air	Deionized Water
Coil Parasitic Capacitance (fF)	85.5	255
Bridge Parasitic Capacitance (fF)	22.3	152
Sensing Capacitance (fF)	244	244
Total Capacitance (fF)	352	651
Coil Inductance (nH)	113	113
Coil Resistance (m Ω)	23.6	23.6
Theoretical Zero-Pressure Resonant Frequency	799 MHz	587 MHz

Electromechanical simulations were performed in COMSOL to estimate the capacitive response of the pressure sensor.

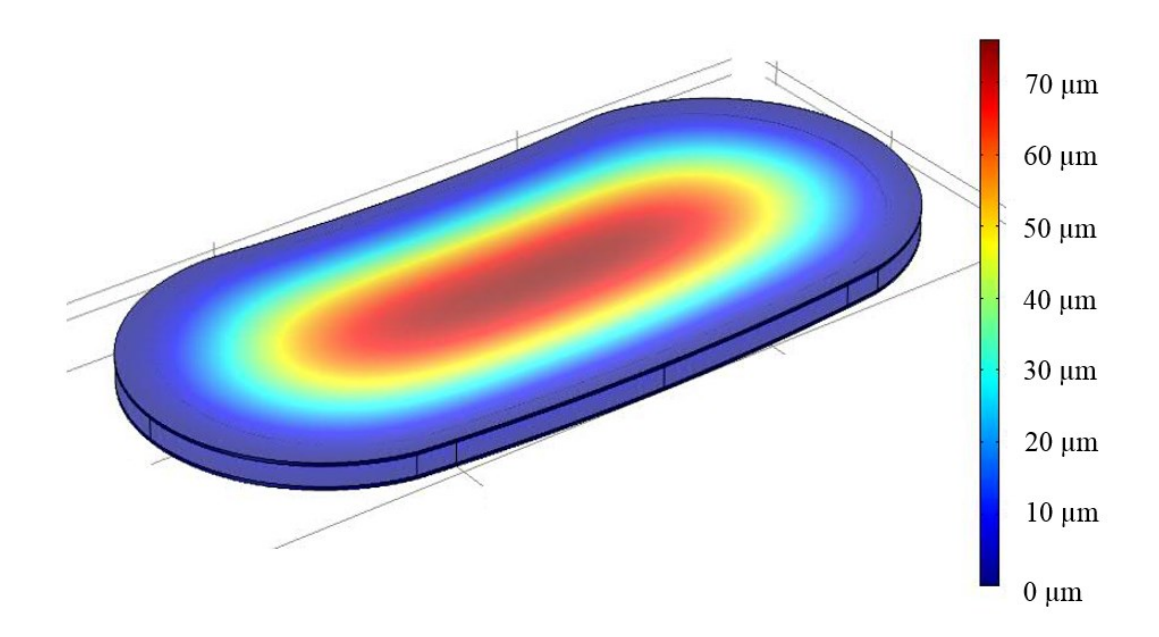


Figure 5-7. Deflection of the capacitive sensing membranes due to an applied pressure

The graphic above shows the deflection of the capacitive chamber in response to an applied pressure. The sensing diaphragms consist of a 500 nm copper layer encased in a 10 μ m Parylene layer. The medium between the diaphragms is air. Fixed constraints are applied at the perimeter of each membrane and uniform pressures ranging from 0 to 100 mmHg are applied to the boundary shown below and the one opposite.

The average deflection of the copper layers with respect to each other, and the corresponding capacitance values are plotted in Figure 5-7. The sensing element capacitance changes with pressure by 47% over the range of 0 to 100 mmHg. Due to parasitic capacitance, this corresponds to a total registered capacitance change of 32% in air and only 18% in water.

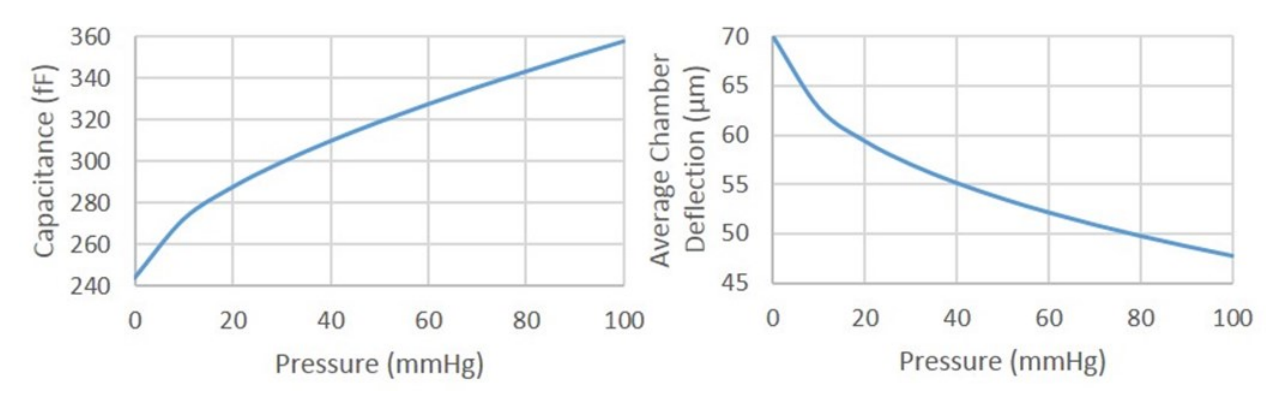


Figure 5- 8. Simulated capacitance versus pressure

Figure 5- 9. Simulated chamber deflection versus pressure

5.3 Testing Setup and Results

Testing was conducted in air, deionized water and isotonic saline. A syringe pump (PHD 2000, Harvard Apparatus) was used as the pressure source for testing. The pressure chamber used for testing (Figure 5-7c) is connected to a 50 mL syringe mounted on the syringe pump. The other end of the test chamber is connected to a water column manometer for deionized water and isotonic saline testing (Figure 5-7b) and a digital pressure sensor air testing (Figure 5-7a). For each medium, pressure was varied from 0 to 100 mmHg in steps of 10 mmHg and the impedance

phase of a reader coil held coaxial to the sensor at a distance of one centimeter (Figure 5-7c) was read using an HP4191A impedance analyzer.

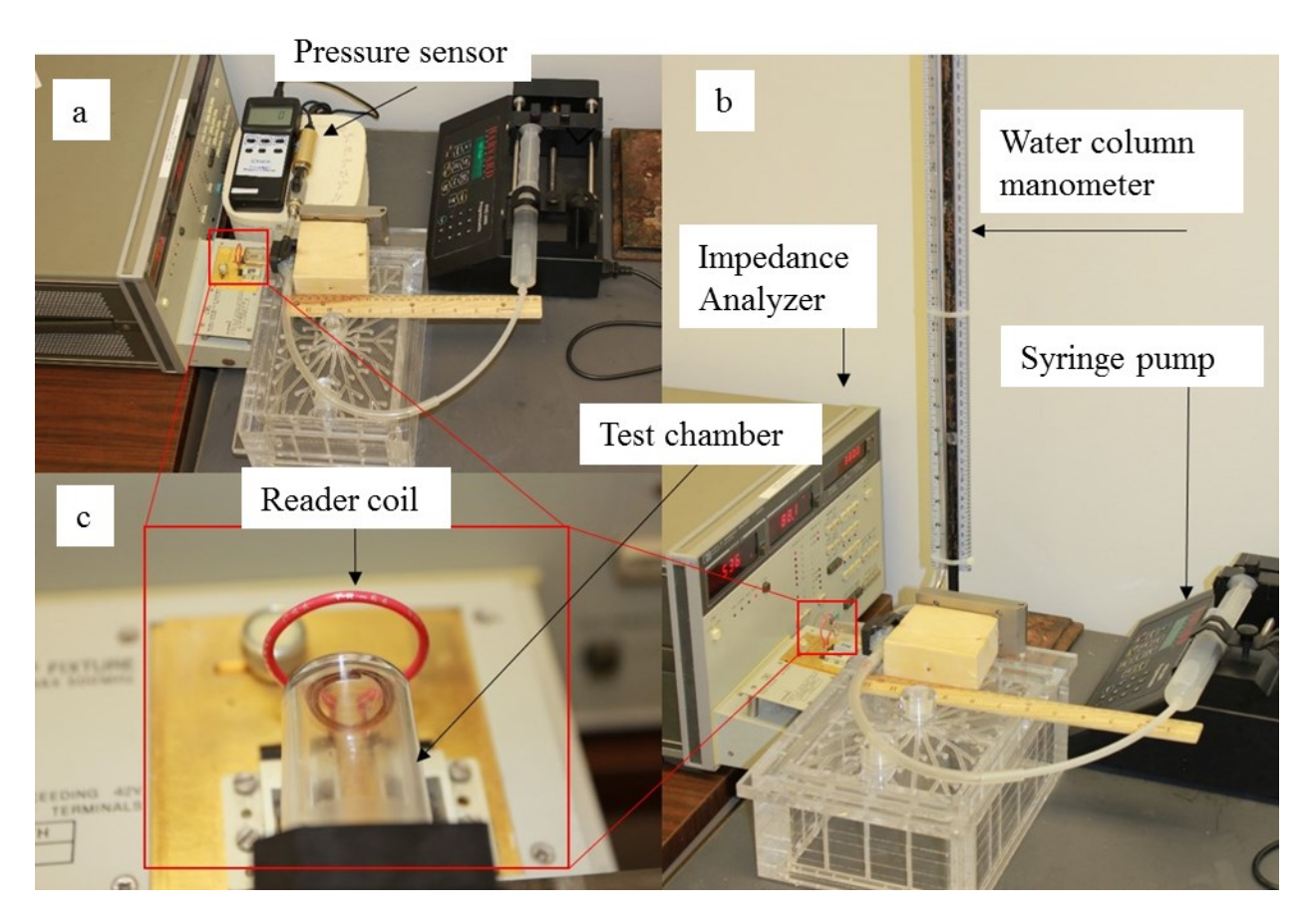


Figure 5- 10. Experimental setup for testing in (a) air and (b) water. (c) Reader coil and test chamber

Raw data from these measurements are plotted in Figure 5-11. These plots show the impedance phase of the reader coil during measurement including the phase dip due to inductive coupling with the sensor. Each curve represents a measurement taken with a different pressure condition. The right-most curves are atmospheric pressure readings and the left-most curves represent readings at 100 mmHg.

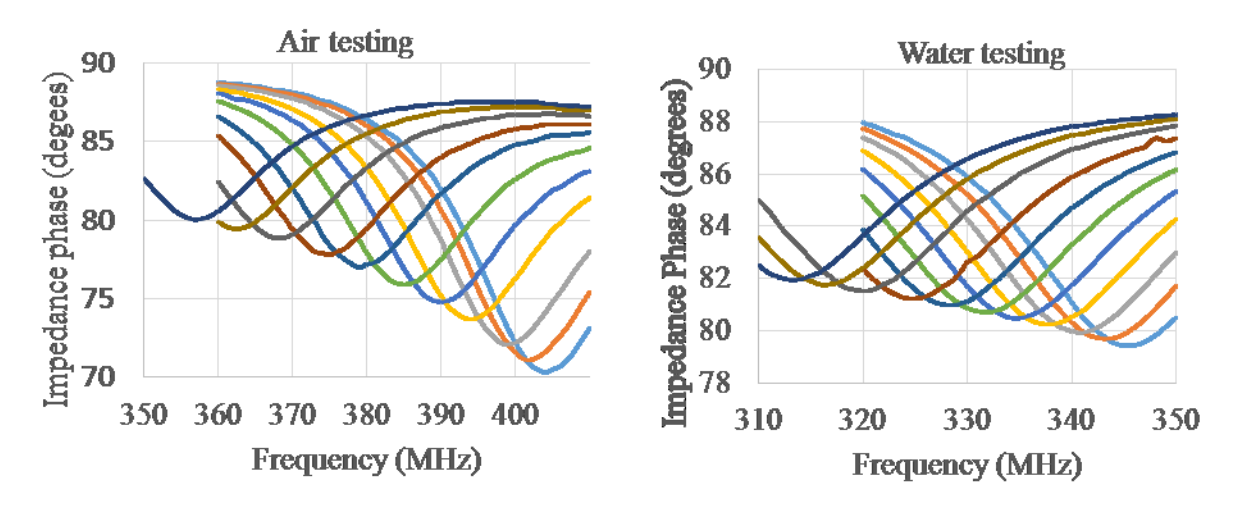


Figure 5- 12. Measured impedance phase curves in air (left) and liquid (right) media

The plots in Figure 5-12 show the frequencies at which phase dip minima for different pressure conditions. These results indicate the sensor operates in a region of high sensitivity and linearity. Telemetry distance testing at zero pressure was also conducted by varying the distance between the reader coil and sensor in increments of 1 mm. A summary of testing results is presented in Table 5-2.

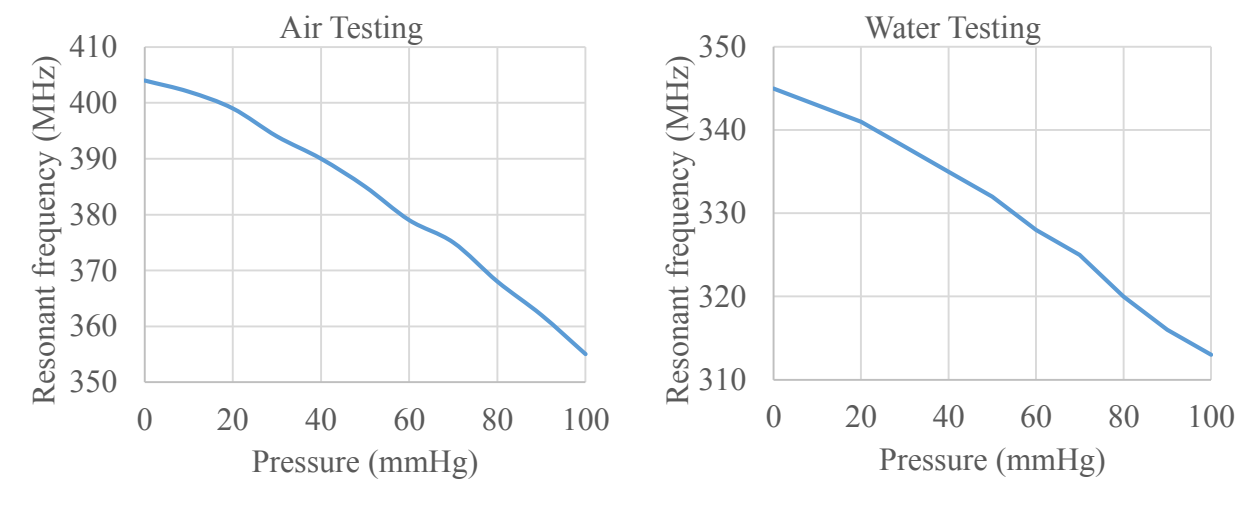


Figure 5- 11. Frequencies at which phase dip minimum occurs as seen in figure 5-11. Data for pressures from 0 and 100 mmHg above atmospheric pressure in air (left) and water (right)

5.4 Summary of Results and Conclusion

Table 5-2. Summary of results

	Minimum	Average	Maximum sensing	Resonant frequency @ 0
	Sensitivity	Sensitivity	distance	mmHg
Air	200	490	3.0 cm	404 MHz
	kHz/mmHg	kHz/mmHg		
DI	200	320	2.5 cm	345 MHz
Water	kHz/mmHg	kHz/mmHg		
Saline	N/A	N/A	2.0 cm	320 MHz

Here the minimum sensitivity indicates the smallest recorded deviation of the resonant frequency deviation between any two pressure measurements. There is a much improved sensitivity and telemetry distance over the version 1 device. The sensor construction using highly flexible, all biocompatible materials make it suitable for animal implantation. This wireless sensor, or a device of very similar design could be a very useful tool for wireless IOP monitoring of laboratory animals in a 1-2 year glaucoma study.

CHAPTER 6: CONCLUSION AND OUTLOOK

This thesis has discussed the design and development of an implantable intraocular pressure sensor. It is larger than most other passive wireless IOP sensors that have been developed, roughly the diameter of the iris. This has enabled a large sensing distance as the inductive coupling necessary for telemetry is highly related to coil size. The device is constructed from just three highly biocompatible materials and is foldable for easy implantation with a small incision. The sensor has achieved both a telemetry distance and sensitivity that make it suitable for animal implantation. The work presented in this thesis demonstrates the feasibility of passive, wireless intraocular pressure sensing to enable accurate, continuous IOP measurements in laboratory animals to further glaucoma research. Despite having met key design and performance goals, some work still remains. First, the sensor could be further improved and refined. Better sensitivity and telemetry range are achievable. Fabrication processes could be further refined to achieve greater throughput and sensor uniformity. Next, or concurrently, a complete platform based on this sensor could be constructed. The sensing platform will include a hand-held or cage- or goggle-mounted reader coil, a unit for sensor readout and data storage and software to analyze readings and process data.

6.1 Readout Unit

Preliminary testing has been conducted with a bench-top impedance analyzer, which is too bulky and expensive for the research applications described in this thesis. Readout units could be constructed entirely from scratch or assembled from proven test equipment already

commercially available. Portable network analyzers would be very effective for this application but are quite expensive. Certain radio test equipment could be used at a more reasonable price point. The MFJ-269 is a portable SWR analyzer, capable of measuring the complex impedance of an inductively coupled circuit with the appropriate dip coils attached. It sells for \$389.00 plus \$24.95 for dip coils. It can measure complex impedance in the range of 1.8-170 MHz [52]. While the MFJ-269 is capable of the measurements needed for this application, it must be hand-tuned to find the sensor resonant frequency. External devices would need to be attached to record measurements and translate a frequency reading to an IOP value.

A readout unit could be constructed for this application that would automatically sweep the frequency range of interest several times and record the average local minimum in the impedance phase. A continuous measurement mode would allow several readings to be made every second for a predetermined amount of time. In the research setting, proximity sensors could be used to prompt the unit to begin taking measurements when the subject moves within range. A suitable readout unit will enable the practical use of the Version II sensor in a research study. The large-scale deployment of such a sensor will depend on the willingness of glaucoma researchers to use larger animal models rather than mice, and the total duration of continuous IOP monitoring needed for a study. A key feature of a successful readout system will be the ability to self-calibrate. By including a mechanism to make several measurement in quick succession as the reader coil-to-sensor separation is varied it would be possible to correct measurement error due to the effect of mutual inductance on the signal being measured. This would provide better frequency resolution and accuracy as well as a greater detectable range, as measurement noise could be filtered during the calibration.

6.2 Remaining Challenges

One drawback of the device size is that it must be implanted in larger animal subjects such as cats, rabbits or pigs. The most widely used laboratory animal for glaucoma research is the mouse, for which passive IOP sensors are not practical due to the very small size of mouse eyes. Active and RFID devices also face significant challenges in the development of wireless IOP sensors for mice models and to date, no fully functional unit has been demonstrated.

Another drawback is that hermetic sealing is impossible with the materials used. No polymer is capable of providing a hermetic seal. The best liquid crystal polymer (LCP) materials provide about one order of magnitude improved hermeticity over Parylene-C but are not truly hermetic. Furthermore, the stiffness and difficulty patterning LCP make its use a challenging proposition for intraocular pressure sensors. Any polymer-based implanted sensor requiring a packaged reference cavity will eventually fail. For this reason, any lifetime animal studies must contain at least some rigid hermetic packaging material, or the sensors must be easily removed or replaced.

6.3 Potential for Human Implantation

One potential avenue for future work is the possibility of developing a wireless pressure sensor that can be implanted in human eyes. Many biomedical devices have been developed for implantation in the human eye. Their surgical procedures are well-established and the risk of complication is fairly low. Of particular interest are phakic implantable contact lenses. These lenses are used to treat severe short-sightedness and can be implanted in the anterior or posterior

chamber of the eye. Only two versions have received FDA approval to date [53], the Visian ICL (Implantable Collamer Lens) [54] and the Verisyse PIOL (Phakic Intraocular Lens) [55].

The Verisyse PIOL was the first available in the US, having been approved in December 2004. It is made from rigid PMMA and is implanted in the anterior chamber just in front of the iris. The rigidity of the device requires a large corneal incision that needs sutures to close after implantation. The incision can sometimes distort the shape of the cornea when it heals, causing astigmatism [56].

The Visian ICL is a flexible lens that is implanted in the posterior chamber, just in front of the natural lens and behind the iris. It can be folded and implanted through a small corneal incision that does not require sutures. While the surgical procedure for this lens is less invasive, the lens sits very close to the natural lens capsule and can cause cataracts [57].

Both lenses have the potential to block aqueous flow through the pupil causing acute glaucoma. A prophylactic peripheral iridotomy (PI) is necessary to make these lenses safe. The PI ensures aqueous humor flow even if the pupil becomes blocked by using a laser to cut a small hole in the iris [58].

Newer designs that will not require PI's are being used in many countries but are still awaiting FDA approval. The AcrySof Cachet angle-supported IOL is in stage III clinical trials in the US [59]. It is a soft, flexible lens that is intended to be implanted in the anterior chamber of the eye. It is anchored to the anterior chamber angle and supported above the pupil by a bridge, preventing pupillary block and eliminating the need for a PI. This device would be an ideal candidate for wireless pressure sensor integration. Its placement in the anterior chamber would enable a better reader coil-to-cornea sensing distance and the sensor could be easily inspected for damage through the transparent cornea. Implantation or removal through a small, self-healing

incision is essential for such a device to enable the sensor to be removed or replaced depending on the needs of the study and the wishes of the patient.

The option must also exist to leave the sensor in the eye after it has stopped functioning. If it becomes medically dangerous to perform another surgery or if the patient chooses to decline additional surgery it is essential that the sensor will not degrade in the biomedical environment and harm the patient. Due to its construction from all-biocompatible materials, the version II sensor could be integrated into a phakic implantable contact lens and implanted in the eye. Once it no longer functions, it becomes just a harmless structural component of the lens and can remain in the eye indefinitely.

APPENDICES

APPENDIX A: Version I Sensor Fabrication Process

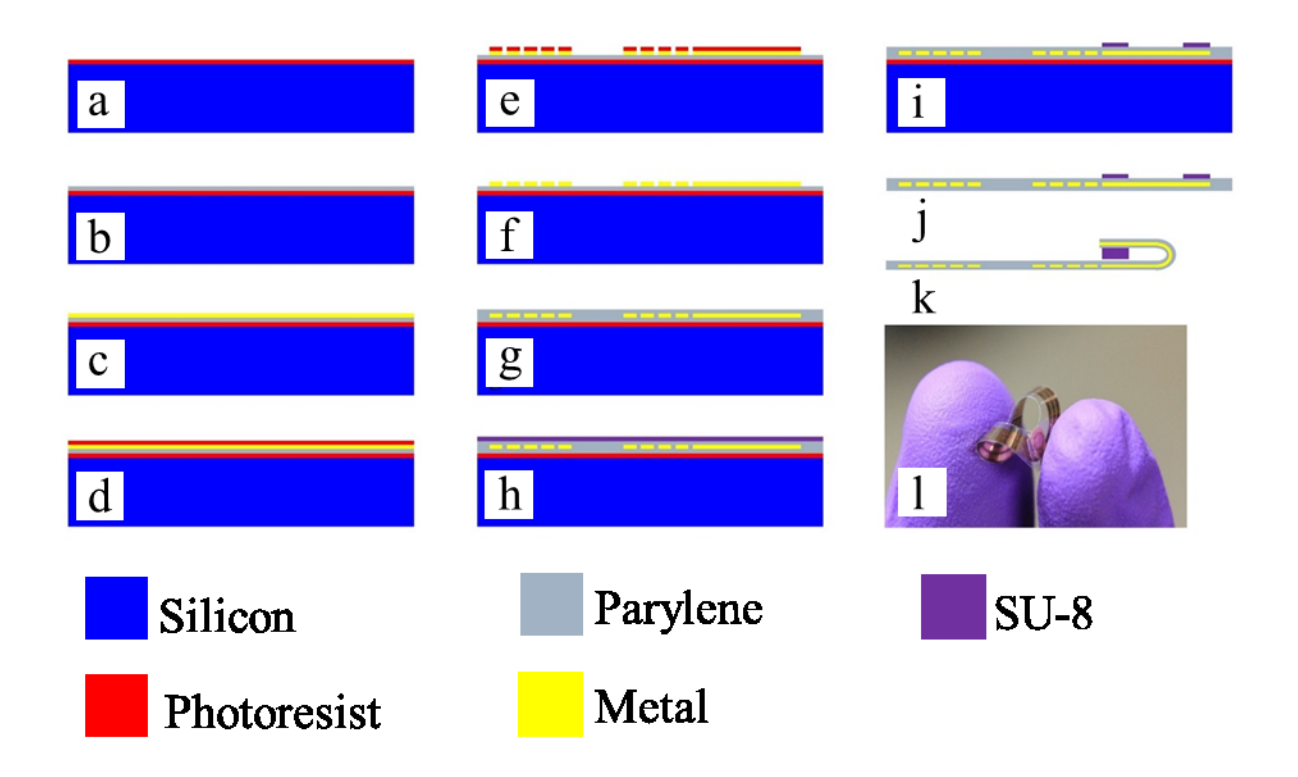


Figure A- 1. Fabrication process flow for the version I sensor

The fabrication process for this sensor is summarized in Fig A-1 above. Steps b-g describe the encapsulation of metal by Parylene, steps h and i involve coating and patterning thick permanent photoresist (SU-8 2050). The final steps, j and k are the release of the device from the substrate and a fold-and-bond process to form the capacitive sensing chamber. Fig A-1(l) shows the flexibility of a finished device.

The first step in this fabrication process is to deposit a 5 µm Parylene layer on a silicon substrate (Figure A-1(b)). Calibration curves and accurate estimates of total deposition chamber surface area are necessary to find a precise relationship between the loaded dimer mass and resulting thickness. For an SCS Labcoter II with standard 12" chamber that relationship works

out to roughly 1.5 g of dimer to yield 1 μ m of thickness. Since this Parylene layer will later be separated from the substrate, poor adhesion is required. The native oxides on a fresh wafer prevent strong Parylene-silicon adhesion. If poorer adhesion is required the wafer can be coated with HMDS or a 2% Micro-90 solution. Alternatively, a thin sacrificial photoresist layer can be used (Fig A.1.a).

5000 Å of copper is then deposited using a thermal evaporator (Edwards Auto 306) as can be seen in step c. A device intended for implantation in a living eye should use gold instead of copper. Gold does not adhere well to Parylene so an adhesion layer of ~50 Å titanium or chromium should be deposited on Parylene before the gold deposition.

A \sim 1.5 µm layer of Shipley 1813 positive photoresist is coated on the metal surface by spinning the wafer at 3000 rpm (Figure A-1(c)). The wafer is softbaked on a hotplate at 110°C for 1 minute. The first mask is placed above the photoresist covered wafer and exposed to UV light in a mask aligner (AB-M) at a dose of 110 mJ/cm². Photoresist is developed in MF319 developer solution for 2 minutes with mild agitation then rinsed with deionized water and dried with nitrogen.

The wafer is placed in a ferric chloride solution until the bare copper is etched away (Figure A-1(e)). The remaining photoresist is dissolved and washed away by rinsing with acetone for 1 minute (Figure A-1(f)). The wafer is then rinsed in isopropyl alcohol for 1 minute to remove acetone residues followed by a 1 minute rinse in deionized water to remove isopropyl alcohol residues. The wafer is then dried with nitrogen and placed in the Parylene deposition for another 5 µm coating as described above (Figure A-1(g)).

Next, a 50 µm layer of SU-8 2050 negative photoresist was deposited on the wafer by spinning at 2500 rpm (Figure A-1(h)). A Q-tip moistened with SU-8 developer solution was held

gently against the side of the wafer as it spun to prevent edge bead formation. A 2-minute soft bake at 65°C was followed by cooling to room temperature and continued baking for 7 minutes at 95°C. SU-8 becomes cross-linked when exposed to UV light, forming a permanent pattern on a substrate. A negative mask was placed above the wafer and aligned to the underlying metal layer. An dose of 250 mJ/cm² was used to expose the SU-8 layer. A post exposure bake of 2 minutes at 65°C followed by 5 minutes at 95°C was conducted. The development time in SU-8 developer solution was 10 minutes. This step removes the unexposed SU-8 (Figure A-1(i)).

Next, devices were cut out and released from the wafer. If a sacrificial photoresist layer was used (Figure A-1(a)) the devices were soaked in acetone to dissolve that layer. Otherwise the devices were soaked in deionized water and the Parylene edges were gently lifted to encourage separation.

Once the devices were released, a fold-and-bond technique was employed (Figure A-1(j)). A small rectangular frame made from adhesive tape is cut to match the outer edge shape of the SU-8 structure on the top capacitor plate. The tape is applied to the bottom SU-8 structure and the two SU-8 structures are folded and bonded together under pressure. To do this the folded sensor was placed on a flat surface between two glass slides. A 500 g mass was placed on the top glass slide and left to sit for 1 hour. After bonding, the interface was coated with a thin layer of PDMS to ensure a good seal.

APPENDIX B: Version II Sensor Fabrication Process

The process of metal encapsulation by Parylene in this device fabrication is exactly as described in Appendix A, Figs. A1.b-g. Rather than using permanent SU-8 photoresist in the next step, AZ4620 was used.

A 30 μm layer of AZ4620 thick positive photoresist is deposited and patterned on the wafer. First, AZ4620 is spun on the wafer at 800 rpm. A Q-tip soaked in acetone is held at the edge of the wafer as it spins to remove the photoresist edge bead. After spinning, the wafer is softbaked at 60°C for 10 minutes, cooled to room temperature then baked at 90 °C for 10 minutes. Another coat of AZ4620 is then applied by repeating this procedure exactly. When the wafer has cooled to room temperature it is placed on the mask aligner stage under the second mask. The photoresist is exposed at a dose of 1200 mJ/cm². Development takes place in AZ351 developer solution diluted 4:1 with deionized water for 20 minutes under mild agitation. The result of this step can be seen in Figure B-1 below.

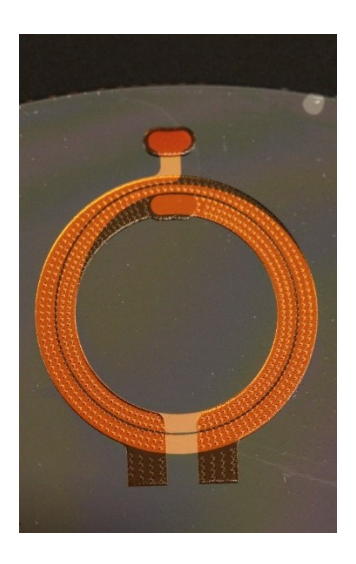


Figure B- 1. Patterned AZ4620 photoresist

The top capacitor plate is then cut and folded onto the bottom plate (Figure B-2).

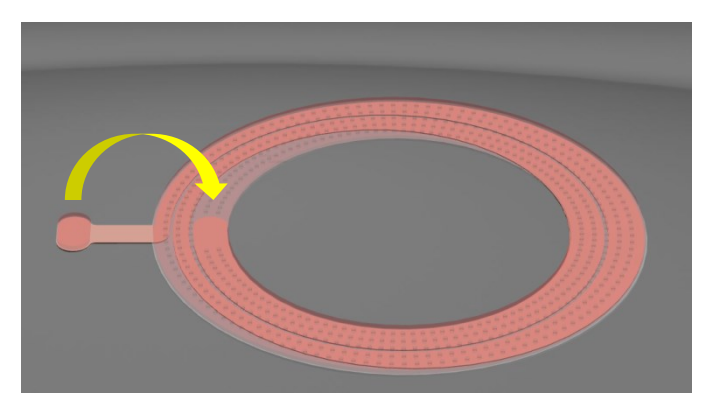


Figure B- 2. Fold-and-bond technique

A glass wafer is place on top of the folded devices to hold them in place and apply some pressure. The wafers are placed on a hotplate for five minutes at 95°C to melt the interface between the folded-together photoresist layers. This step is critical. If the temperature is too high or too much pressure is applied, the glass slide will sink into the resist and destroy the patterns. If the temperature is too low, the interface will not fully melt and the subsequent Parylene deposition will result in a near complete coating of the interface, ruining the sensors. Figure B-3 is a picture of one sensor directly after bonding.



Figure B- 3. Device after elimination of photoresist interface by melting

The sensors are then carefully cut and released from the substrate and suspended on a thin wire in the Parylene deposition system. A final 5 µm Parylene layer is deposited (Figure B-4). After the final Parylene deposition, the ends of the structure are cut with a razor blade to expose the encapsulated photoresist. They are soaked in warm acetone for 48 hours in a sealed container at 50°C to remove the photoresist (Figure B-5). The devices are then soaked in isopropyl alcohol for 8 hours at 60 °C and left overnight in deionized water at 70°C. They devices sit between lint-free disposable towels for 4 hours in a slight vacuum of 1-2 inH₂O at 60°C to dry. Once dry, the edges that had been cut to release the photoresist are creased and folded over. This crease is made permanent by stacking weights on it and baking for 1 hour at 150°C in a vacuum oven. This does not seal the device, it only makes smaller the opening into the Parylene channel. Some PDMS is then dabbed onto the folded sections. The devices are placed in a vacuum oven with no applied temperature under slight vacuum until bubbles can be seen escaping through the PDMS. The vacuum chamber is purged and a small amount of PDMS is forced into the channel. The devices are removed from the vacuum oven and placed on a hotplate for 5 minutes at 90°C to cure the PDMS. A completed device is pictured in Fig B.6.

Some devices were then encapsulated in PDMS. This was done by dipping whole devices in PDMS then sitting them on a glass slide. After 2 hours most of the bubbles have escaped and the devices are cured in a vacuum oven at 60°C for 1 hours. Lastly, they are separated from the glass slides with tweezers and deionized water and trimmed with a razor blade if necessary.

BIBLIOGRAPHY

BIBLIOGRAPHY

- [1] Glaucoma Research Foundation, Glaucoma facts and stats, www.glaucoma.org/glaucoma/glaucoma-facts-and-stats.php (Accessed 10/11/13).
- [2] Kent, C. "IOP: managing the fluctuation factor," Review of Ophthalmology. Vol. 11, Num. 26. June 13, 2011.
- [3] Mansouri, K.; Sharaway, T.; Continuous intraocular pressure monitoring with a wireless ocular telemetry sensor: initial clinical experience in people with open angle glaucoma," British Journal of Ophthalmology
- [4] Lawrence, M.G.; Kramarevsky, N.Y.; Christiansen, S.P.; Wright, M.M.; Young, T.L.; Summer, C.G.; "Glaucoma following cataract surgery in children: surgically modifiable risk factors," Transactions of the American Ophthalmologic Society, Volume 103:44-46 Dec. 2005.
- [5] Moeller, E.; Blocker, T.; Esson, D.; Madsen, R.; Postoperative glaucoma in the Labrador Retriever: incidence, risk factors, and visual outcome following routine phacoemulsification," Veterinary Ophthalmology, Volume 14(6): 385-94 Nov. 2011.
- [6] Visian ICL, Visian ICL, http://visianinfo.com/about-visian-icl/icl-procedure/, (Accessed 9/3/13).
- [7] IOP Implandata Ophthalmic Products, 24h intraocular pressure measurement, http://implandata.com/24h.html, (Accessed 10/21/13).
- [8] Fred Hollows Foundation. "Anatomy of the eye." http://www.hollows.org.au/eye-health/anatomy-eye, (Accessed 4/1/2012).
- [9] The Mayo Clinic. Glaucoma treatments and drugs, www.mayoclinic.com/health/glaucoma/treatments-and-drugs (Accessed 9/29/13).
- [10] Stein, J.D.; Challa, P.; Scott, I.U.; Fekrat, S.; "Diagnosis and treatment of normal-tension glaucoma," EyeNet Magazine., 200702.
- [11] Chihara E.; "Assessment of true intraocular pressure: the gap between theory and practical data," Survey of Ophthalmology. Volume (3):203-18, June 2008.

- [12] ksums.net. "Index of /files/Archive/4th/428/Ophtha/B1/OSCE/A1 OSCE." http://www.ksums.net/files/Archive/4th/428/Ophtha/B1/OSCE/A1%20OSCE/, (Accessed 10/1/2013).
- [13] Friedenwald, J.S.; "Tonometer calibration; an attempt to remove discrepancies found in the 1954 calibration scale for Schiotz tonometers," Trans Am Acad Ophthalmol Otolaryngol, Volume 61(1):108-22, 1956.
- [14] McBain, E.H.; "Tonometer calibration. II. Ocular rigidity," AMA Arch Ophthalmol, Volume 60(6):1080-91, 1958.
- [15] McBain, E.H.; "Tonometer calibration; determination of Pt formula by use of strain gauge and recording potentiometer on enucleated normal human eyes," AMA Arch Ophthalmol, Volume 57(4):520-31, 1959.
- [16] Kniestedt C.; Lin S.; Punjabi O.; Stamper R.L.; "Tonometry through the ages.," Surv Ophthalmol. Volume 53(6):568-91, Dec 2008.
- [17] Kornblueth W.; Jampolsky A.; Tamler E.; Marg E.; "Activity of the oculorotary muscles during tonometry and tonography: An electromyographic study," Arch Ophthalmol Volume 62:555-61, 1959.
- [18] Krakau C.E.; Wilke K.; "On repeated tonometry," Acta Ophthalmol (Copenh) Volume 49(4):611-4, 1959.
- [19] Carolina Valdivia MD. "Can An Applanation Tonometry Test Cause Eye Infections?" http://www.glaucoma-eye-info.com/applanation-tonometry.html, (Accessed 10/1/2013)
- [20] Ehlers N.; Bramsen T.; Sperling S.; "Applanation tonometry and central corneal thickness," Acta Ophthalmol (Copenh) Volume 53(1):34-43, 1979.
- [21] Rosa N.; Cennamo G,.; Breve M.A.; La Rana A.; "Goldmann applanation tonometry after myopic photorefractive keratectomy," Acta Ophthalmol Scand Volume 76(5):550-4, 1998.
- [22] Fernandes P.; Diaz-Rey J.A.; Queiros A.; "Comparison of the ICare rebound tonometer with the Goldmann tonometer in a normal population," Ophthalmic Physiol Opt Volume 25(5):436-40, 2005.
- [23] Cervino A.; "Rebound tonometry: new opportunities and limitations of non-invasive determination of intraocular pressure," Br J Ophthalmol Volume 90:1444–1446, 2006.
- [24] Davies L.N.; Barlett H.; Mallen E.A.; Wolffsohn J.S.; "Clinical evaluation of rebound tonometer," Acta Ophthalmol Scand Volume 84(2):206-9, 2006.

- [25] Garcia Resua C.; Gonzalez Meijome J.M.; Gilino J.; Yebra Pimentel E.; "Accuracy of new ICare rebound tonometer vs. other portable tonometers in healthy eyes," Optom Vis Sci Volume 83(2):102-7, 2006.
- [26] Nakamura M.; Darhad U.; Tatsumi Y.; "Agreement of rebound tonometer in measuring intraocular pressure with three types of applanation tonometers," Am J Ophthalmol Volume142(2):332-4, 2006.
- [27] Geeta Eye Clinic and Surgery Centre. "Tonometry." http://geetaeyeclinic.com/services/diagnostic/tonometry/, (Accessed 9/25/2013)
- [28] Kanngiesser H.; Kniestedt C.; Robert Y.C.; "Dynamic contour tonometry: presentation of a new tonometer," J Glaucoma Volume 14(5):344-50, 2005.
- [29] Kristopher May, O.D. "A Roundup of 8 Recent Diagnostic Devices." http://www.revoptom.com/content/d/therapeutics/c/17158/dnnprintmode/true/?skinsrc=% 5Bl%5Dskins/ro2009/pageprint&containersrc=%5Bl%5Dcontainers/ro2009/simple, 5/24/2006 (Accessed 9/28/2013)
- [30] Doyle A.; Lachkar Y.; "Comparison of dynamic contour tonometry with goldmann applanation tonometrz over a wide range of central corneal thickness," J Glaucoma Volume 4(4):288-92, 2005.
- [31] Pache M.; Wilmsmeyer S.; Lautebach S.; Funk J.; "Dynamic contour tonometry versus Goldmann applanation tonometry: a comparative study," Graefes Arch Clin Exp Ophthalmol Volume 243(8):763-7, 2005.
- [32] Kaufmann C.; Bachmann L.M.; Thiel M.A.; "Intraocular pressure measurements using dynamic contour tonometry after laser in situ keratomileusis," Invest Ophth Vis Science Volume 44(9):3790-4, 2003.
- [33] Kniestedt C.; Lin S.; Choe J.; "Clinical comparison of contour and applanation tonometry and their relationship to pachymetry," Arch Ophthalmol Volume 123(11):1532-7, 2005.
- [34] Kotecha A.; White E.T.; Shewry J.M.; Garway-Heath D.F.; "The relative effects of corneal thickness and age on Goldmann applanation tonometry and dynamic contour tonometry," Br J Ophthalmol Volume 89(12):1572-5, 2005.
- [35] Olga, Savinova, Sugiyama Fumihiro, Martin Janice, Tomarev Stanislav, Paigen Beverly, Smith Richard, and John Simon. "Intraocular pressure in genetically distinct mice: an update and strain survey." BMC Genetics 2.

- [36] Johnson, Thomas V., and Stanislav I. Tomarev. "Rodent models of glaucoma." Brain research bulletin 81, no. 2 (2010): 349-358.
- [37] Gelatt, K. N., and E. O. MacKay. "Distribution of intraocular pressure in dogs." Veterinary Ophthalmology 1, no. 2-3 (1998): 109-114.
- [38] Sensimed. Sensimed triggerfish provides an automated recording of continuous ocular dimensional changes over 24 hours. www.sensimed.ch/en/products/sensimed-triggerfishr.html (Accessed 10/2/13).
- [39] Edward, Chu and Ania, Hamp. "IOP goes bump in the night" (Review of Optometry) [online] 4/5/2011 www.revoptom.com (accessed 10/20/13).
- [40] Weber A.J.; "Autocrine and paracrine interactions and neuroprotection in glaucoma," Cell Tissues Res Volume 353:219-230, 2013.
- [41] Makoto A.; James L.; Weinreb R.N.; "Twenty-four-hour pattern of mouse intraocular pressure," Experimental Eye Research Volume 77 (6):681-686, December 2003.
- [42] Lin, J.C.-H.; Yu Zhao; Po-Jui Chen; Yu-Chong Tai, "High quality factor Parylene-based intraocular pressure sensor," Nano/Micro Engineered and Molecular Systems (NEMS), 2012 7th IEEE International Conference on , vol., no., pp.137,140, 5-8 March 2012
- [43] Chen, G.; Ghaed, H.; Haque, R.; Wieckowski, M.; Yejoong Kim; Gyouho Kim; Fick, D.; Daeyeon Kim; Mingoo Seok; Wise, K.; Blaauw, D.; Sylvester, D., "A cubic-millimeter energy-autonomous wireless intraocular pressure monitor," Solid-State Circuits Conference Digest of Technical Papers (ISSCC), 2011 IEEE International, vol., no., pp.310,312, 20-24 Feb. 2011
- [44] Chitnis, G.; Maleki, T.; Samuels, B.; Cantor, L.B.; Ziaie, B., "A Minimally Invasive implantable Wireless Pressure Sensor for Continuous IOP Monitoring," Biomedical Engineering, IEEE Transactions on, vol.60, no.1, pp.250,256, Jan. 2013.
- [45] Ning Xue; Sung-Pil Chang; Jeong-Bong Lee, "A SU-8-Based Microfabricated Implantable Inductively Coupled Passive RF Wireless Intraocular Pressure Sensor," Microelectromechanical Systems, Journal of, vol.21, no.6, pp.1338,1346, Dec. 2012
- [46] Unigarro, E.A.; Sanz, D.A.; Arciniegas, A.; Ramirez, F.; Segura-Quijano, F., "High resolution implantable wireless MEMS intraocular pressure sensor," Health Care Exchanges (PAHCE), 2013 Pan American, vol., no., pp.1,3, April 29 2013-May 4 2013
- [47] Po-Jui Chen; Rodger, D.; Yu-Chong Tai; Humayun, M., "Spiral-tube Parylene intraocular pressure sensor," Micro Electro Mechanical Systems, 2005. MEMS 2005. 18th IEEE International Conference on , vol., no., pp.311,314, 30 Jan.-3 Feb. 2005

- [48] HIS GlobalSpec. "Vacuum Gauges and Instruments Information." http://www.globalspec.com/learnmore/manufacturing_process_equipment/vacuum_equipment/vacuum_gauges, (Accessed 10/10/2013)
- [49] Byungjoo Kang; Hoyong Hwang; Soo Hyn Lee; Ji Yoon Kang; Joung-Hu Park; Chulhun Seo; Changkun Park; "A wireless intraocular pressure sensor with variable inductance using a ferrite material," Journal of Semiconductor Technology and Science, Volume 13(4): 355-360, Aug. 2013.
- [50] Po-Jui Chen; Rodger, D.C.; Saati, S.; Humayun, M.S.; Yu-Chong Tai, "Microfabricated Implantable Parylene-Based Wireless Passive Intraocular Pressure Sensors,"

 Microelectromechanical Systems, Journal of, vol.17, no.6, pp.1342,1351, Dec. 2008
- [51] F. E. Terman, Radio Engineers' Handbook. New York: McGraw-Hill, 1943
- [52] MFJ Enterprises catalog, http://www.mfjenterprises.com/Product.php?productid=MFJ-269 (Accessed 10/14/13)
- [53] Devices@FDA Catalog, http://www.accessdata.fda.gov/scripts/cdrh/devicesatfda/index.cfm (Accessed 10/12/13)
- [54] Visian ICL information page, http://visianinfo.com/ (Accessed 10/12/13)
- [55] Abbott Medical Optics, Verisyse product page, http://www.amo-inc.com/products/cataract/refractive-iols/verisyse-phakic-iol (Accessed 10/12/13)
- [56] Michelle Dalton. (2012, February). IOLs Determining your surgically induced astigmatism [Online]. Available: http://eyeworld.org/article.php?sid=6217
- [57] Dermot McGrath. (2006, March). Excellent visual outcomes for ICL, but cataract formation still a problem [Online]. Available: http://www.escrs.org/publications/eurotimes/06march/pdf/excellentvisualoutcomes.pdf
- [58] Michelle Dalton. (2012, December). Device focus Phakic IOLs and peripheral iridotomy [Online]. Available: http://eyeworld.org/article.php?sid=6610
- [59] AcrySof Cachet information page, http://www.acrysofcachet.ca/phakic-lenses.asp (Accessed 10/14/12)